Check for updates

JGR Oceans

RESEARCH ARTICLE
10.1029/2025JC023411

Synoptic Pathways of Mid-Depth Salinity Maximum Intrusions in the South Brazil Bight

D. A. Silva[1], A. Gangopadhyay[2], D. K. Sasaki[1,3], M. Dottori[1], I. C. A. da Silveira[1], W. C. Belo[4], and R. P. Martins[4]

[1]Instituto Oceanográfico, Universidade de Sao Paulo, São Paulo, Brasil, [2]School for Marine Sciences and Technology, University of Massachusetts, New Bedford, MA, USA, [3]Department of Marine and Environmental Sciences, Northeastern University, Nahant, MA, USA, [4]Centro de Pesquisas, Desenvolvimento e Inovação Leopoldo Américo Miguez de Mello - CENPES/PETROBRAS, Cidade Universitária da Universidade Federal do Rio de Janeiro, Rio de Janeiro, Brazil

Abstract Cross-shelf exchanges play a crucial role in distributing heat, salt, and biogeochemical properties between the continental shelf and the open ocean. Among the processes shaping these exchanges, the intrusion of warm and salty waters (mid-depth Salinity Maximum, S_{max}) remains poorly understood in the South Brazil Bight (SBB). We present observational evidence of S_{max} intrusions in the Northeastern SBB (NE-SBB) based on hydrographic observations collected between February and March 2022. Using a multi-platform observational data set combined with Lagrangian particle tracking, we show that S_{max} originate north of the study region and were advected southward primarily by the Brazil Current (BC). Two dominant advective pathways are identified: (a) a southwestward along-shelf route associated with a non-meandering BC, and (b) a cross-shelf pathway driven by the interaction between the BC meander and the cyclonic Cabo Frio Eddy that is intensified by the presence of an eddy dipole. Once S_{max} reaches the shelf break, its penetration onto the continental shelf is wind-driven, mid-depth onshore counterflow during upwelling-favorable conditions, as suggested by the Burger number analysis higher than 1. These results highlight a two-step mechanism for S_{max} intrusions in the NE-SBB, where mesoscale dynamics govern remote delivery to the shelf edge, while wind-driven circulation and stratification regulate onshore penetration and vertical structure. By elucidating the pathways and mechanisms of S_{max} intrusions, this study advances the understanding of cross-shelf exchanges in the SBB and emphasize the importance of remotely forced processes in shaping the thermodynamics and biogeochemistry of subtropical continental shelves.

Plain Language Summary In this study, we investigate how warm and salty subsurface waters, known as Salinity Maximum intrusions (S_{max}), reach the continental shelf in the South Brazil Bight (SBB). Using observations from February to March 2022 and numerical tracking of water parcels, we show that these waters originate north of the study region and are transported southward by the Brazil Current (BC). Two main pathways are identified: a southwestward along-shelf route under a smooth BC regime, and a cross-shelf pathway driven by the interaction between the BC and a rotating ocean feature called the Cabo Frio Eddy, which can be intensified by interacting with another eddy rotating in the opposite direction. Once at the shelf edge, wind-driven currents during upwelling-favorable conditions promote subsurface onshore transport. Together, these results reveal a two-step mechanism in which mesoscale ocean features deliver salty waters to the shelf break, and wind-driven circulation carries them onto the continental shelf, with important implications for coastal stratification, nutrient supply, and marine productivity in the SBB.

Key Points:

- Observational evidence that mid-depth Salinity Maximum intrusions in the South Brazil Bight are advected preferentially from north
- Brazil Current (BC)–Cabo Frio Eddy interaction delivers Salinity Maximum intrusions to the shelf edge; winds inject them into the shelf
- An enhancement by eddy dipole interaction and advection through a non-meandering BC are also identified as secondary processes

Supporting Information:

Supporting Information may be found in the online version of this article.

Correspondence to:

D. A. Silva,
danilo2.silva@usp.br

Citation:

Silva, D. A., Gangopadhyay, A., Sasaki, D. K., Dottori, M., da Silveira, I. C. A., Belo, W. C., & Martins, R. P. (2026). Synoptic pathways of mid-depth salinity maximum intrusions in the South Brazil Bight. *Journal of Geophysical Research: Oceans*, *131*, e2025JC023411. https://doi.org/10.1029/2025JC023411

Received 10 SEP 2025
Accepted 29 AUG 2026

Author Contributions:

Conceptualization: D. A. Silva
Data curation: D. A. Silva
Formal analysis: D. A. Silva, A. Gangopadhyay
Funding acquisition: M. Dottori, W. C. Belo, R. P. Martins
Investigation: D. A. Silva, A. Gangopadhyay, D. K. Sasaki
Methodology: D. A. Silva, A. Gangopadhyay, D. K. Sasaki

© 2026 Petrobra, Universidade de São Paulo and The Author(s). Journal of Geophysical Research: Oceans published by Wiley Periodicals LLC on behalf of American Geophysical Union.
This is an open access article under the terms of the Creative Commons Attribution License, which permits use, distribution and reproduction in any medium, provided the original work is properly cited.

1. Introduction

Cross-shelf exchanges are critical processes that influence the distribution of heat, salt, pollutants (Brink, 2016) and biogeochemical properties (Cossarini et al., 2015; Liu et al., 2010) between the continental shelf and the open ocean. Western boundary currents, such as the Brazil Current (BC), play an important role in these exchanges because of their dynamic nature and the transport of warm, saline waters poleward along the western margins of ocean basins.

The Northeastern South Brazil Bight (NE-SBB, Figure 1) exhibits a secondary maximum of eddy kinetic energy (EKE) in the South Atlantic Basin (refer to Figure 1 from Rocha & Simoes-Sousa, 2022). This elevated EKE is related to the recurrent presence of cyclonic eddies generated off Cabo Frio (Cabo Frio Eddy, CFE) and Cabo de São Tomé (Cabo de São Tomé Eddy, CTE) (Silveira et al., 2023; Uchoa et al., 2023). The generation of these

Project administration: M. Dottori, I. C. A. da Silveira, W. C. Belo, R. P. Martins
Software: D. A. Silva
Supervision: A. Gangopadhyay, M. Dottori, I. C. A. da Silveira
Validation: D. A. Silva
Visualization: D. A. Silva
Writing – original draft: D. A. Silva
Writing – review & editing: A. Gangopadhyay, D. K. Sasaki, I. C. A. da Silveira

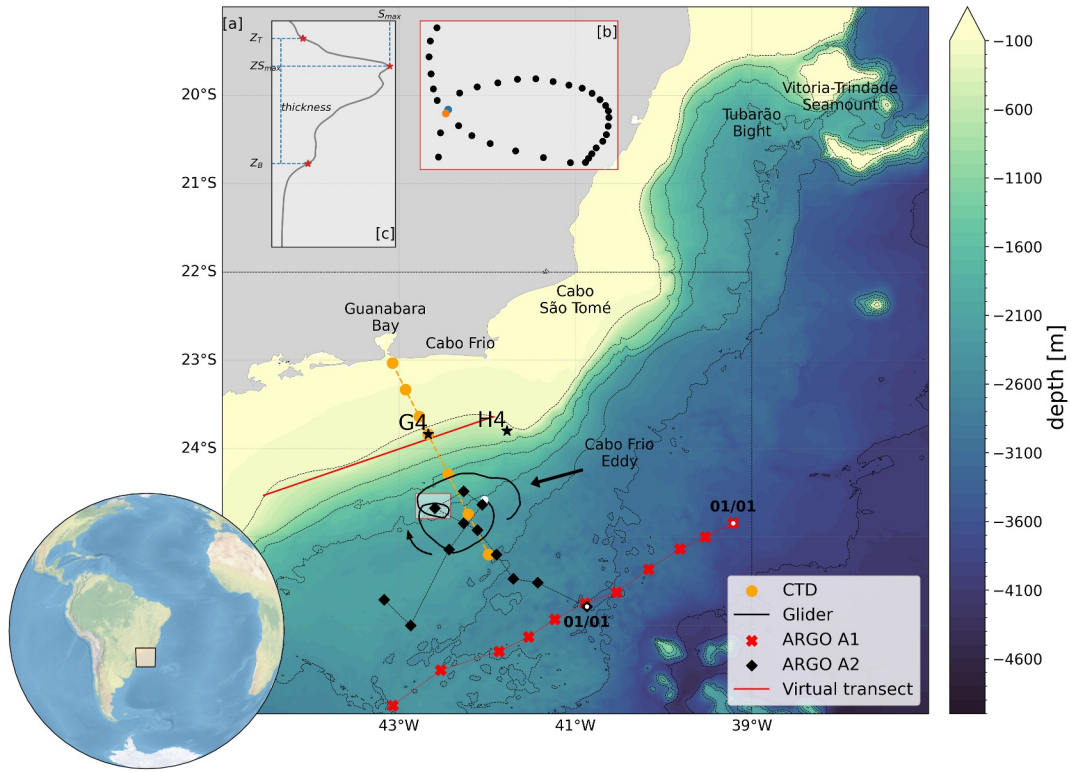


Figure 1. (a) Northeastern South Brazil Bight (NE-SBB) with observational locations in orange representing CTD profiles; red and black represent ARGO profiles along Line A1 (3901549) and Line A2 (3901225), respectively; the continuous black line represents the Slocum Glider SG19 track depicting the Cabo Frio Eddy; white dots represent the starting point of the ARGOS and Glider's path, the red line represents the along-shelf-edge transect used for cross-shelf velocity calculations. The bathymetric data, marked in color, were extracted from the GEBCO 2019 data set (Weatherall et al., 2015), and the contours represent the −100, −200, −1,000, −2,000, −4,000, and −5,000 m isobaths. Panel (b) highlights a specific part of the glider's path in which a loop was performed. The orange and blue dots are two specific profiles measured during the glider's path. (c) Sample absolute salinity profile showing the salinity maximum (S_{max}) characteristics: ZS_{max} is the depth of the S_{max}; Z_T and Z_B are the depths of the top and bottom boundaries, respectively; and *thickness* is the difference between them. The S_{max} characteristics were extracted based on the adaptations of the Lentz (2003) algorithm of Silva et al. (2023).

eddies results from the topographic interactions of the poleward BC and the equatorward Intermediate Western Boundary Current (Luko et al., 2022). The development of meanders and cyclonic eddies influences cross-shelf exchanges (Calil et al., 2021; Combes et al., 2023), in addition to wind-driven cross-shelf circulation (Brink, 2016; Castro, 2014). The on-shelf outcome of these processes over the shelf edge leads to the development of thermohaline intrusions, that is, inversions of temperature and salinity (Ruddick & Kerr, 2003). Although such structures may appear gravitationally unstable, the opposing effects of temperature and salinity on seawater density frequently compensate, allowing intrusions to remain neutrally buoyant (Stern, 1967).

Thermohaline intrusions can be observed near the bottom, which influence the region by injecting cold and nutrient rich waters (South Atlantic Central Water, SACW) onto the shelf, thus increasing primary productivity and atmospheric CO_2 sequestration (Oliveira et al., 2019). However, recent studies have shown a separate intrusion occurring at mid-depth levels that injects warm and salty water onto the shelf (Tropical Water, TW, Campos et al., 2000; Castro, 2014; Silva et al., 2023). These intrusions, defined as a peak in subsurface salinity and often called salinity maximum intrusions (hereinafter referred to as S_{max}, Gordon & Aikman III, 1981), sometimes even block the pathway between the nutrient rich waters near the bottom and the euphotic zone (Dottori et al., 2023; Silva et al., 2023), thus affecting the biogeochemical properties of the shelf and the transport of larvae from the ocean (Namiki et al., 2017; Vilanova et al., 2026). These mid-depth salinity maximums, S_{max}, are generally observed to be associated with seasonal pycnocline (Lentz, 2003; Silva et al., 2023) and are responsible for the injection of salt onto the shelf. For example, on the Middle Atlantic Bight (MAB, a shelf region of the North Atlantic along the U.S. east coast), S_{max} drives the onshore salt flux, providing half of what is

21699291, 2026, 11, Downloaded from https://agupubs.onlinelibrary.wiley.com/doi/10.1029/2025JC023411 by Capes, Wiley Online Library on [10/11/2026]. See the Terms and Conditions (https://onlinelibrary.wiley.com/terms-and-conditions) on Wiley Online Library for rules of use; OA articles are governed by the applicable Creative Commons License

21699291, 2026, 11, Downloaded from https://agupubs.onlinelibrary.wiley.com/doi/10.1029/2025JC023411 by Capes, Wiley Online Library on [10/11/2026]. See the Terms and Conditions (https://onlinelibrary.wiley.com/terms-and-conditions) on Wiley Online Library for rules of use; OA articles are governed by the applicable Creative Commons License

Table 1
Overview of the Observational Data Sets Used in This Study, Specifying the Source (Institution, Product Name, or Reference), Extracted Variables, and Analysis Periods

Data set	Reference	Variables	Period
CTD	Moreira et al. (2023)	T,S	March 2022
ARGO	IFREMER (2025)	T,S	January–March 2022
Glider	Alves dos Santos et al. (2015)	T,S	February–March 2022
AVISO	CMEMS (2024b)	Gridded ADT	Jan– Mar, 2022
AVISO	CMEMS (2024a)	Along track ADT	
ERA5	Hersbach et al. (2018)	Wind stress	
GLORYS12V1	Jean-Michel et al. (2021)	u, v, T, S	
MERGE	Rozante et al. (2010)	Precipitation	
AVHRR	–	SST	
META3.1exp DT	Pegliasco et al. (2022)	Eddy track(x, y, t)	

Note. ADT denotes Absolute Dynamic Topography.

necessary to balance the freshwater input and maintain the annual average salinity in the region (Gordon & Aikman III, 1981).

Although thermohaline intrusions are linked to several mechanisms, such as wind- and eddy-driven circulation (Gawarkiewicz et al., 1990, 2025; González-Pola et al., 2007; Li et al., 2012; Malan et al., 2020; Ruiz-Castillo et al., 2019; Silver et al., 2023), internal waves (Hopkins et al., 2012) and baroclinic pressure gradients (Aikman, 1984; Posmentier & Houghton, 1978), the drivers of S_{max} intrusions are still unresolved in the SBB. Considering the dominance of eddies and wind in shaping cross-shelf exchanges (Calil et al., 2021; Combes et al., 2021, 2023), one might expect that both processes play an important role in developing them. In this study, we investigate the interaction between the dynamics of BC and its eddying meanders and wind-driven circulation and how they might help advect S_{max} from remote offshore regions all the way to the NE-SBB (Figure 1). This investigation is motivated by the observation of multiple S_{max} events advected toward the NE-SBB in March 2022, when the last cruises of the Santos Project–Santos Basin Environmental Characterization–coordinated by PETROBRAS (Moreira et al., 2023) were conducted. The set of sampling cruises was named SANAGU2022.

Here, we present observational evidences that the features found during the research cruises were remotely advected from offshore locations onto the NE-SBB. The sources and pathways of these S_{max} signals were investigated using satellite observations, global reanalysis (GLORYS12V1) and Lagrangian analysis. The manuscript is structured as follows: Section 2 describes the data set used and methods applied; Section 3 presents our results and show preferential S_{max} pathways of advection; Section 4 discusses the interaction between BC dynamics and wind and presents a set of Lagrangian analysis to aid in interpreting the advective pathways and; Section 5 summarizes our main findings.

2. Material and Methods

2.1. Hydrographic Data Set

In this study, we use a diverse set of data from several sources, including in situ measurements, remotely sensed products and global numerical reanalysis (as summarized in Table 1).

The SANAGU2022 sampling was carried out in March 2022, sampling the entire SBB, as described in Moreira et al. (2023). Although multiple transects were made on the NE-SBB during the cruise, in this work we only considered the central transect, off Guanabara Bay (Figure 1, orange markers), as intrusions were only observed along this transect. The transect was sampled twice in 2 weeks: the first sample occurred between 5 and 14 March, and the second was performed between 23 and 28 March. CTD profiles measurements were taken with SBE 911 Plus probe, with stations aligned approximately perpendicular to the coast (orange dashed line in Figure 1).

21699291, 2026, 11, Downloaded from https://agupubs.onlinelibrary.wiley.com/doi/10.1029/2025JC023411 by Capes, Wiley Online Library on [10/11/2026]. See the Terms and Conditions (https://onlinelibrary.wiley.com/terms-and-conditions) on Wiley Online Library for rules of use; OA articles are governed by the applicable Creative Commons License

Quality control and processing methods were applied using a modified version of the Python-CTD package (Dottori et al., 2023; Fernandes, 2014). In the processing workflow, we removed spikes, averaged the data into 1 *m* bin, and applied a 7-point (21-point) window Hanning filter to smooth the profiles over the shelf (slope). This processing is similar to the one applied by Silva et al. (2023) and Dottori et al. (2023) on the same continental shelf and by da Silveira et al. (2023) for the slope casts.

We used ARGO float profiles and a Slocum Glider data set to complement the CTD data set and provide a broader spatial and temporal context for the observed $S_{\max}$ intrusions. The temporal and spatial filtering of the data set resulted in two ARGO profilers: 3901549 and 3901225, defined hereafter as A1 and A2, respectively (Figure 1). From these instruments, we extracted profiles with a quality flag of 1 or 2, indicating "good data" or "probably good data" (ARGO, 2025). The Glider data set was obtained at the ProjetoAzul portal (http://www.projetoazul.eco.br/, accessed in May 2023). The metadata available within the data set presents quality control, which was used to select the information quality flag 0, meaning "good data." Hydrographic properties, such as absolute salinity, potential density and Brunt-Vaisalla frequency, from all vertical profiles were derived from in situ measurements, using the Gibbs SeaWater (GSW) oceanographic toolbox of Thermodynamic Equation of SeaWater 2010 (TEOS-10, McDougall & Barker, 2011) through the GSW Python package (Firing et al., 2021).

2.2. Characteristics of Salinity Maximum Intrusions

An algorithm of salinity intrusions (Lentz, 2003) adapted for the SBB thermodynamics (Silva et al., 2023) provided the intrusion characteristics used in this work. These characteristics are illustrated in Figure 1c. The maximum salinity is defined as $S_{\max}$ and its corresponding vertical position is $ZS_{\max}$. The profile is only defined as a $S_{\max}$ event when the vertical gradient (ΔS) exceeds the threshold of 0.1g kg^{-1}, following Silva et al. (2023). The vertical limits (Z_T and Z_B) were defined as the depth at which salinity decreases to 75% of its vertical range relative to the peak value, considering the range between the maximum salinity and the lowest salinity observed in the upper or lower layer. From these limits, we only calculated the thickness of the $S_{\max}$, but we acknowledge it is also possible to extract other useful characteristics. For further description of the adaptations, the reader is referred to Silva et al. (2023). Here, we define $S_{\max}$ signal for the features found in open ocean and $S_{\max}$ intrusion for those found within the continental shelf.

2.3. Altimeter Data Set

Sea surface elevation and geostrophic velocities derived from a global altimeter product complement our analysis. These data sets are available on the Copernicus Marine Environment Monitoring Service (CMEMS) website. Here, we used both L4 grid products (CMEMS, 2023b) and L3 along track altimeter data (CMEMS, 2023a) to reconstruct mesoscale scenarios. The gridded absolute dynamic topography (ADT) product has a 0.25° spatial resolution at daily frequency and merges data from all available altimeter missions, using an optimal interpolation to construct the final product. Zonal and meridional geostrophic currents were calculated based on geostrophic balance (Equations 1 and 2). Along track altimeter was used to compute geostrophic velocity normal to the track, which allows the visualization of mesoscale features with higher resolution. This technique provides velocities with an average resolution of 7 km and was recently applied to investigate the dynamics of the Gulf Stream and its relation to intrusions of salinity maximum in this region (Silver et al., 2022). We selected tracks that crossed relevant features, such as the BC and eddy dipoles present on the continental slope of SBB during February and March of 2022 resulting in a total of 19 tracks (see Figure 4). Cross-track velocities (U_{ct}) were calculated using ADT fields along the track using Equation 3.

$$U_g = -\frac{g}{f}\frac{\Delta ADT}{\Delta y}(\text{-gridded ADT}) \quad (1)$$

$$V_g = \frac{g}{f}\frac{\Delta ADT}{\Delta x}(\text{-gridded ADT}) \quad (2)$$

$$U_{ct} = -\frac{g}{f}\frac{\Delta ADT}{\Delta s}(\text{-track ADT}) \quad (3)$$

21699291, 2026, 11, Downloaded from https://agupubs.onlinelibrary.wiley.com/doi/10.1029/2025JC023411 by Capes, Wiley Online Library on [10/11/2026]. See the Terms and Conditions (https://onlinelibrary.wiley.com/terms-and-conditions) on Wiley Online Library for rules of use; OA articles are governed by the applicable Creative Commons License

where, g is the acceleration of gravity, f is the Coriolis parameter and "Δs" is the spatial resolution of the grid along the path (≈7 km).

The Mesoscale Eddy Trajectories Atlas multi-satellite delayed-time product (META3.1exp, Pegliasco et al., 2022) allowed us to explore the eddy activity during the period. This data set provides the position, speed, amplitude and other information about the eddies, detected with the py-eddy tracker algorithm (Mason et al., 2014) applied over the ADT of the gridded AVISO product. This data set was filtered to select cyclones and anticyclones from January to March 2022, over the domain of interest.

2.4. Additional Data Sets

To provide context on the meteo-oceanographic conditions, several data sets were used to complement the ones described in previous sections. Sea surface temperature (SST) data were obtained from the Advanced Very High Resolution Radiometer Level 3 data set, with a 4-km resolution at daily frequency (Saha et al., 2018). Precipitation was retrieved from the MERGE data set (Rozante et al., 2010), which combines satellite precipitation data from the Tropical Rainfall Measuring Mission with surface observations from meteorological stations over the South American continent. This product results in maps of daily accumulated precipitation with a 12-km spatial resolution. The meteorological conditions were also analyzed using hourly wind stress at the surface, retrieved from the fifth generation reanalysis (ERA5 hereafter, Hersbach et al., 2018), provided by the European Center for Medium-range Weather Forecasts. This data set has a 0.25° resolution and combines numerical model results and observations from satellites, buoys and meteorological stations via data assimilation (Hersbach et al., 2018). We used currents (zonal and meridional), temperature and salinity from daily averages of the 1/12° Global Ocean Physics Reanalysis (GLORYS12V1; Jean-Michel et al., 2021) to explore the advection of subsurface high salinity features. GLORYS12V1 assimilates reprocessed and quality controlled satellite observations of sea level anomaly, sea surface temperature, as well as in situ observations of temperature and salinity (Jean-Michel et al., 2021). From these data sets, we extracted information from January to March 2022.

2.5. Dynamical Computations

2.5.1. Cross-Shelf Edge Exchanges

The Ekman Transport based on wind stress allowed the identification of the cross-shelf response to winds during January and March 2022 (Equation 4, Brink, 2016; Gangopadhyay, 2022):

$$T_{Uek} = \frac{\tau_y^{ERA5}}{f\rho}$$
$$T_{V\,ek} = -\frac{\tau_x^{ERA5}}{f\rho} \quad (4)$$

where T_{Uek} and $T_{V\,ek}$ is the zonal and meridional Ekman transport, τ_x and τ_y the zonal and meridional wind stress components, $\rho = 1028$ kg m^{-3} is the water density.

The cross-shelf geostrophic velocity was calculated along the 200-m isobath, which is defined as a virtual transect (red line in Figure 1) and indicates here the shelf break limit; the bathymetry for this analysis was obtained from the GEBCO data set (Weatherall et al., 2015). Both cross-shelf geostrophic velocity and Ekman transport were rotated using an average angle of 55°.

2.5.2. Additional Computations

Assuming that $S_{\max}$ intrusions correlate with the maximum stratification in a water column, and thus are associated with the pycnocline (Silva et al., 2023), it is helpful to calculate the mixed layer depth (MLD) to investigate whether intrusion signals are consistent with previous intrusions observed in the region. The MLD was determined through the gradient density criteria (Lorbacher et al., 2006), with a threshold of 0.025 kg m^{-3}. This is relevant as the temperature criteria alone (e.g., Boyer Montégut et al., 2004) may not be representative of MLD where salinity gradients are important in the SBB (Silveira et al., 2023; Sasaki et al., 2024).

21699291, 2026, 11, Downloaded from https://agupubs.onlinelibrary.wiley.com/doi/10.1029/2025JC023411 by Capes, Wiley Online Library on [10/11/2026]. See the Terms and Conditions (https://onlinelibrary.wiley.com/terms-and-conditions) on Wiley Online Library for rules of use; OA articles are governed by the applicable Creative Commons License

Table 2
Summary of Lagrangian Experiments Performed, Along With Seeding Center and Depth, Number of Particles Launched (n) Distributed Over a 1° Squared Box and Date of Release

Experiment	Center	Vertical position	n	Date	[B/F]
BPI	42.77°W, 23.64°S	50 m depth	100	2022-03-27	B
BPII	42.77°W, 23.64°S	25.5 kg m^{-3} isopycnal	100	2022-03-27	B
FPE	39°W, 26.5°S	50 m depth	100	2022-01-01	F
FPN	40°W, 22°S	50 m depth	100	2022-01-01	F

Note. For PBI and PBII, the location, depth and date of release are related to the last vertical profiles in which S_{max} was detected. PBI and PBII are backpropagation experiments using the 3D GLORYS12V1 hydrodynamical field and the 25.5 kg m^{-3} isopycnal velocity, respectively. Experiments FPE and FPN are forward propagation experiments, using the 3D GLORYS12V1 hydrodynamical field, with particles released at locations selected from the PBI results, to the east and north of the region of interest, respectively. On these experiments, particles were released at 50-m depth on January 1st and run for 90 days. The B/F columns indicates whether the experiment is a Backward (B) or Forward (F) simulation.

To understand the response of cross-shelf circulation to upwelling favorable winds at the shelf break, we computed the slope Burger number (Equation 5), using observed vertical profiles near the shelf edge (depicted in Figure 1):

$$Bu = \frac{N * \alpha}{f} \tag{5}$$

where N is the Brunt-Vaisalla frequency and α is the topographic gradient ($\alpha = \frac{dh}{dx'}$, where x' is the direction of the cross-isobath), extracted from GEBCO in the locations closest to the CTD casts used. The Burger number indicates whether the cross-shelf circulation response to wind stress will be barotropic or baroclinic (Clarke & Brink, 1985; Lentz & Chapman, 2004). This distinction is crucial for understanding the vertical structure of the cross-shelf circulation induced by wind stress. In particular, when $Bu \geq 1$, the onshore current opposite the favorable wind-driven circulation caused by upwelling will take place in subsurface levels, above the bottom boundary layer (Lentz & Chapman, 2004).

2.6. Lagrangian Experiments

Lagrangian experiments were conducted to assess probable pathways leading to the S_{max} observed on SBB. We chose the Parcels-code v2.4 model (Delandmeter & Van Sebille, 2019) to carry out these experiments, due to its wide applications to understand trajectories in the ocean using outputs of general ocean circulation models (Dawson et al., 2023; Seijo-Ellis et al., 2023; Vallès-Casanova et al., 2022). The advection of virtual particles employs a fourth-order Runge-Kutta iteration scheme (Delandmeter & Van Sebille, 2019), using velocity fields from GLORYS12V1 (Jean-Michel et al., 2021). This product provides daily hydrodynamic fields, in a 0.08° horizontal resolution, assimilating large observational data sets as has been used for Lagrangian analysis on different studies (Amorim et al., 2025; Belonenko et al., 2024; Fedorov et al., 2021). The Lagrangian experiment setup uses a built-in extra module that deletes particles that reaches any closed boundary, avoiding accumulation at the boundaries. Table 2 summarizes the Lagrangian experiments and the their characteristics, which were selected based on the S_{max} observations. The setup is explained in more detail in Section 3.4. The results are presented as concentration maps that compute the total number of particles passing by each grid cell during the integration of the experiment, normalized by the total amount of particles released.

3. Results

3.1. Salinity Maximum Intrusions During March 2022

The hydrographic transects reveal differences in oceanographic conditions during 2 weeks in the Northeast region of the SBB (NE-SBB). We identified an S_{max} intrusion signal along the transect during the first week (Figure 2a, named A), with a well-defined intrusion over the shelf edge between 25 and 50 m depth. This feature corresponded to a 25 m thick S_{max} intrusion of saltier waters ($S > 37$ g kg^{-1}), crossing the isopycnals (white dashed lines in Figure 2a). A relatively fresher extension of the same intrusion was found on the inner shelf, with a

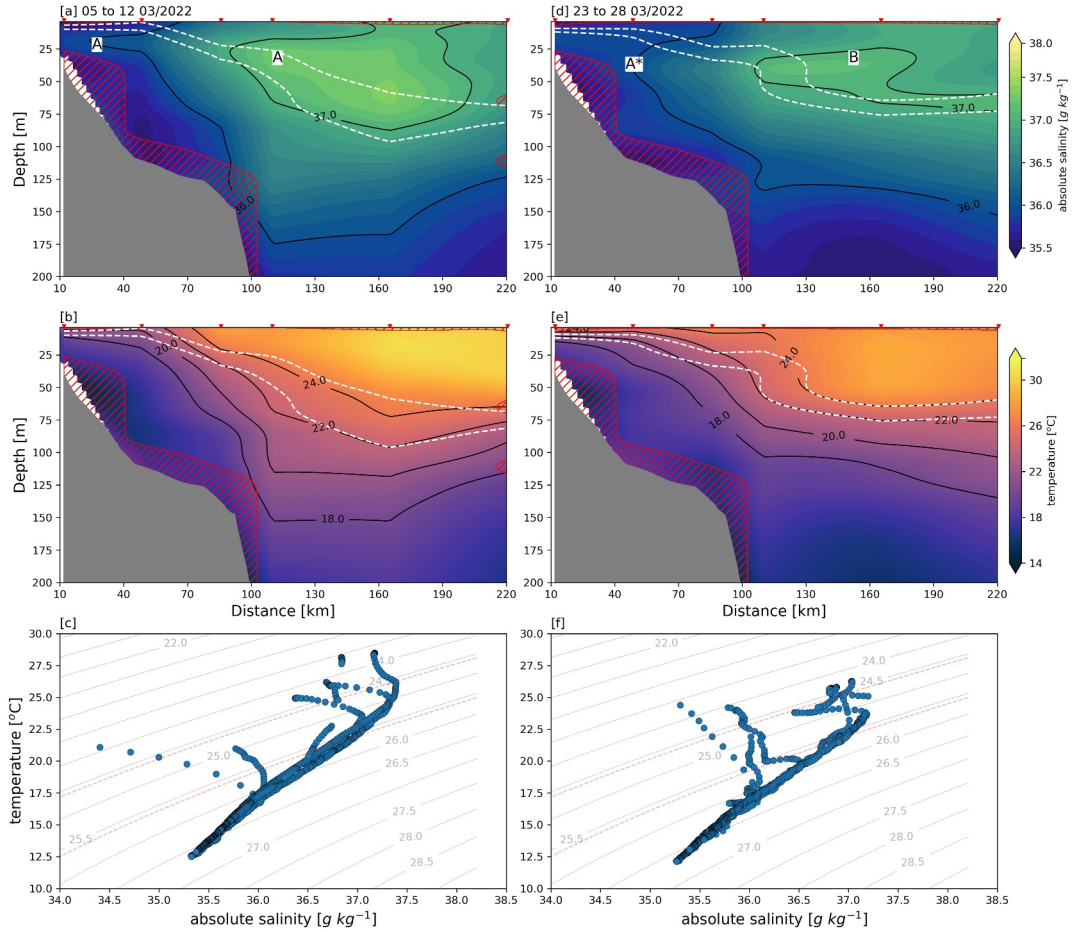


Figure 2. Transects of absolute salinity (top panels) and temperature (middle panels), reconstructed with optimum interpolation using CTD profiles obtained during the first (left) and second (right) research cruises, whose locations are indicated by the orange dotted line in Figure 1. Bottom panels show the corresponding TS diagrams for each campaing. In panels (a), (b), (d) and (e) black contours denote isolines of the plotted property, while white contours indicate 25 and 25.5 kg m^{-3} isopycnals. The *x*-axis represents the horizontal distance from the coastline (km), and the *y*-axis indicates depth (*m*). Red dots at the surface mark the locations of the vertical profile used in the reconstruction. The red hashed area near the bottom areas highlights regions with high normalized error variance (>0.001), where the interpolated fields should be interpreted with caution. Letters A and B identify distinct S_{max} intrusions, and A* denotes an intrusion undergoing erosion. In panels (c) and (f) the isopycnal lines of 24.6 and 25.6 kg m^{-3} are also shown for reference in dashed red lines.

thickness of approximately 20 m and waters with 36 g kg^{-1}. The freshening is caused by the dilution or diffusion of the intrusion as it propagates toward the coast (Silva et al., 2023). Along the first transect, an intense difference in temperature was found at the surface, varying from 20°C, in the inner shelf, to over 30°C offshore (Figure 2b). Near the bottom, water colder than 18^{o}C indicate the presence of the relatively cold and nutrient-rich South Atlantic Central Water (SACW), as indicated by the TS diagram (Figure 2c). This water mass is found throughout the year in the area as response to the offshore surface Ekman Transport forced by northeast winds (Castro, 2014; Cerda & Castro, 2014; Dottori et al., 2023). The near bottom onshore advection also uplifts isopycnals toward the coast (Figures 2a–2c). At the region offshore the shelf break, water warmer than 25°C with salinity higher than 36 g kg^{-1} was found, indicating the presence of Tropical Water (TW) (Castro, 2014; Cerda & Castro, 2014).

After 2 weeks, the second transect (Figures 2d–2f) reveals a slightly different hydrographic condition. This transect shows the presence of a S_{max} signal coming onto the shelf, with waters 2 g kg^{-1} fresher than the previous case (therefore, named as B). During the second cruise, intrusion B occupied depth levels above the 25 kg m^{-3} isopycnal, except for the region near the shelf edge between 100 and 150 km from the coast, where the feature crosses the isopycnals. Intrusion A (Figure 2a) retreated toward the shelf edge, suggesting the erosion of its

21699291, 2026, 11, Downloaded from https://agupubs.onlinelibrary.wiley.com/doi/10.1029/2025JC023411 by Capes, Wiley Online Library on [10/11/2026]. See the Terms and Conditions (https://onlinelibrary.wiley.com/terms-and-conditions) on Wiley Online Library for rules of use; OA articles are governed by the applicable Creative Commons License

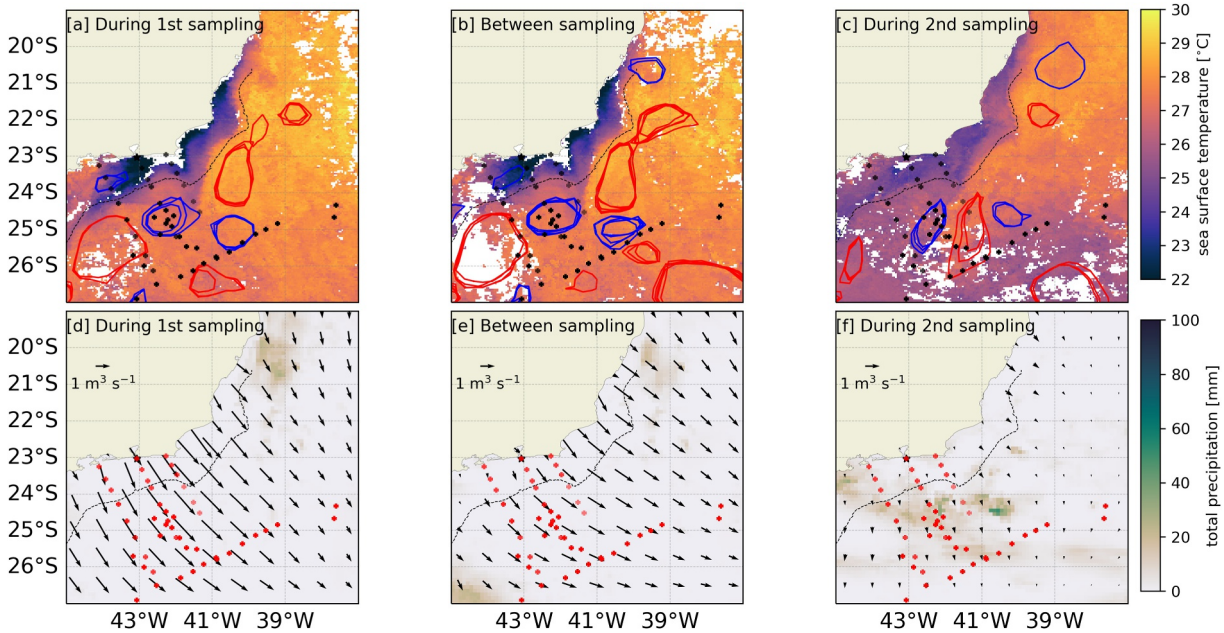


Figure 3. Plain view of the averaged satellite-derived Sea surface temperature condition presented in the top panels in colors (data from Advanced Very High Resolution Radiometer), for (a) the period from 5 to 14 March (1st sampling), (b) between cruises (from 15 to 22 March) and (c) for the second sampling (23–28 March). These panels are superimposed by cyclonic (blue) and anticyclonic (red) eddies (obtained from Meta3.1exp DT) detected during each period. Bottom panels presents the accumulated precipitation (from the MERGE data set) for each period with Ekman transport (calculated from ERA5 wind stress) as black vectors. Black (at the upper panels) and red (at the bottom panels) dots represent the hydrographic data set correspondent to all CTD and ARGO profiles, as indicated in Figure 1 (check Section 2.1 for more details).

intrusion (A* in Figure 2d). The temperature structure (Figure 2e) also changed between the two transects. This transects shows a weaker cross-shelf temperature gradient, with waters relatively warmer on the inner shelf (around 26°C) and slightly colder offshore (around 28°C), as indicated in the TS diagram for this cruise (Figure 2f).

Satellite-derived sea surface temperature (SST) shows a cross-shelf difference of approximately 4°C, with temperatures below 22°C on the shelf and above 26°C offshore (Figure 3a), also observed in the CTD profiles (Figure 2a). This horizontal contrast suggests cold water uplift driven by seasonal upwelling-favorable north-easterly winds (Dottori et al., 2023; Emílsson, 1961). During the second transect (Figure 3c), the cross-shelf temperature difference is weaker, around 2^{o}C. These changes are consistent with in situ surface temperature patterns observed along the cruise transect (Figures 2b and 2e), despite some discrepancies between satellite and in situ near-surface measurements (Pereira et al., 2020).

3.2. SST Patterns and Mesoscale Circulation

Here, we evaluate the influence of mesoscale features and the Ekman transport on the shelf break and slope environment, associated with the S_{max} signals observed during the cruises. The weather conditions during both transects were different and may be responsible for the differences in SST. During the first cruise, the presence of upwelling-favorable winds (Figure 3d) likely reduced shelf temperatures, while weak cloud coverage favored an increase in offshore SST, contributing to the relatively larger gradient observed. During the second cruise, the passage of a frontal system a few days prior to the observations contributed to reducing the SST field throughout the domain, weakening the Ekman transport due to the reduction of wind intensity (Figure 3f).

The mesoscale signals detected in remotely sensed images were associated with the presence of S_{max} during the period. For instance, SST patterns resembled a CFE signal in both cruises (Figure 3), offshore the NE-SBB (centered in, approximately, 25°S and 42°W). The geostrophic currents (Figure 4) showed an interaction between a CFE and an anticyclonic eddy, centered at approximately 24.5°S and 41.5°W, between February and early March (Figures 4a–4c). This interaction led to intense currents, reaching up to 0.6 ms^{-1}. Its influence over the SST field is depicted mainly as a cold water tongue at the eastern edge of the eddy (Figures 3a and 3b, at the

21699291, 2026, 11, Downloaded from https://agupubs.onlinelibrary.wiley.com/doi/10.1029/2025JC023411 by Capes, Wiley Online Library on [10/11/2026]. See the Terms and Conditions (https://onlinelibrary.wiley.com/terms-and-conditions) on Wiley Online Library for rules of use; OA articles are governed by the applicable Creative Commons License

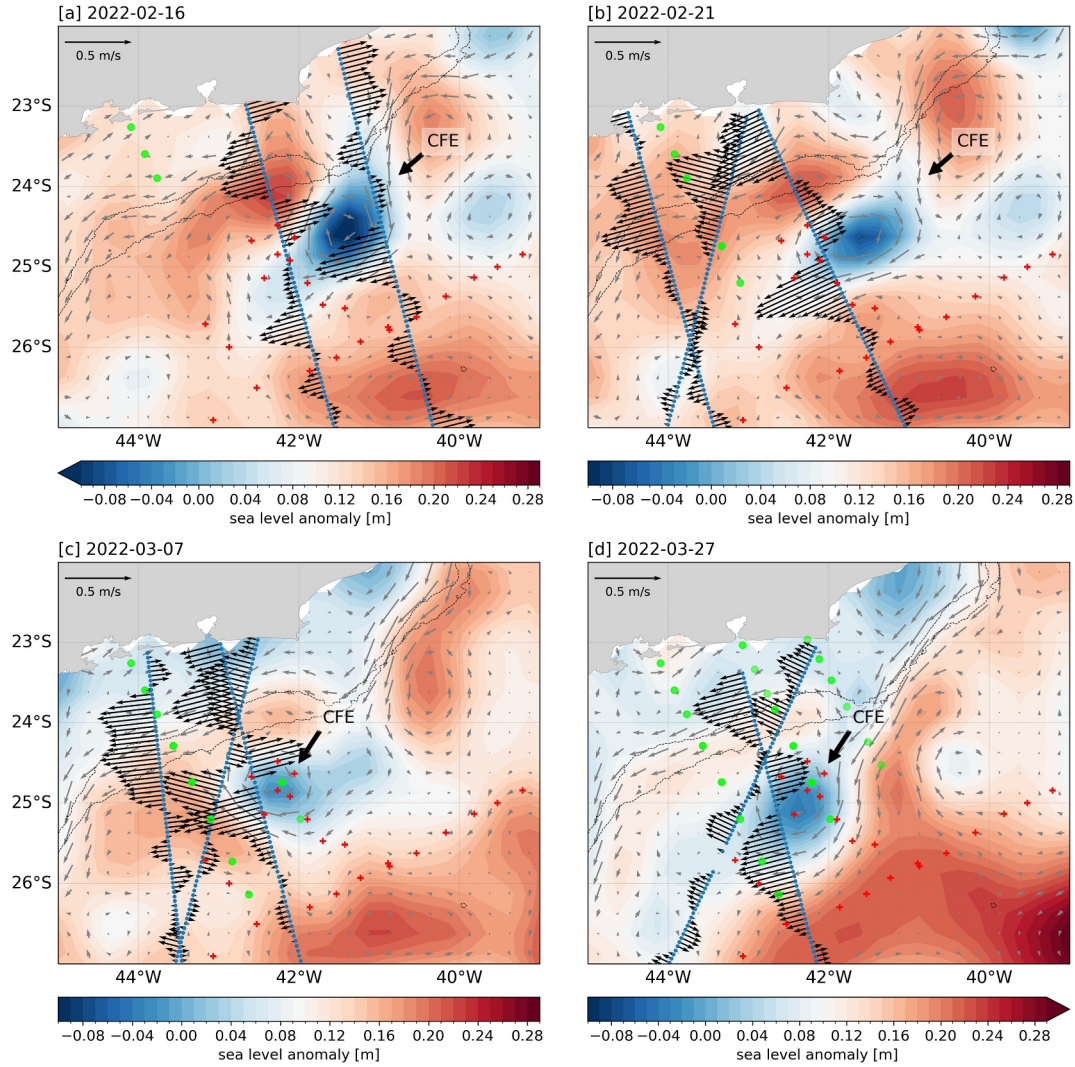


Figure 4. Zoomed plain view (black dashed square on Figure 1) of the sea surface elevation anomalies (in colors and contour) from gridded AVISO for (a) February 16, (b) February 21, (c) March 7 and (d) March 27. Geostrophic velocity fields overlaid the plots in gray vectors, for gridded AVISO, and computed using along-track altimeter absolute dynamic topography in black vectors. Green markers represent locations of CTD profiles obtained by the time of each plot and red markers are the locations of the ARGO profiles. Big black arrows on all panels spot the location of the Cabo Frio Eddy and the anticyclonic eddy observed during the period. The red dots indicate the profilers originated from the ARGO data set. The green dots are the CTD profiles obtained during the cruises, each subpanel only presents the profiles sampled prior to the day associated with the sea level anomalies and geostrophic velocity. They were used as reference for the mesoscale features observed.

same location). At the end of March, the BC split in two branches at 24°S and 41.5°W (Figure 4d), with one branch flowing along the shelf edge, westward, and another branch flowing southwestward. This second branch meanders around a weaker CFE, and then part of this branch attaches back to the shelf edge near 24°S and 42.3°W. The influence of the meander on the cross-shelf currents is observed on the cross-shelf geostrophic current Hovmoller along a transect following the 200-m isobath (Figure S1 of Supporting Information S1). This analysis shows two centers of intense shoreward currents occurring between January and February and during March (Figure S1 of Supporting Information S1). The projected shoreward geostrophic current occur between 24.5°S and 24.0°S, the same spot where the BC meander attaches back to the shelf edge. Therefore, it is expected that mesoscale activity plays an important role over the cross-shelf exchanges, in addition to upwelling-favorable winds response.

Altimetry-derived geostrophic velocities were preferred over fixed-depth reanalysis velocities for characterizing the mesoscale circulation because sea surface height integrates the barotropic and baroclinic pressure signal over approximately the upper 100 m of the water column, providing a more complete representation of the depth-

21699291, 2026, 11, Downloaded from https://agupubs.onlinelibrary.wiley.com/doi/10.1029/2025JC023411 by Capes, Wiley Online Library on [10/11/2026]. See the Terms and Conditions (https://onlinelibrary.wiley.com/terms-and-conditions) on Wiley Online Library for rules of use; OA articles are governed by the applicable Creative Commons License

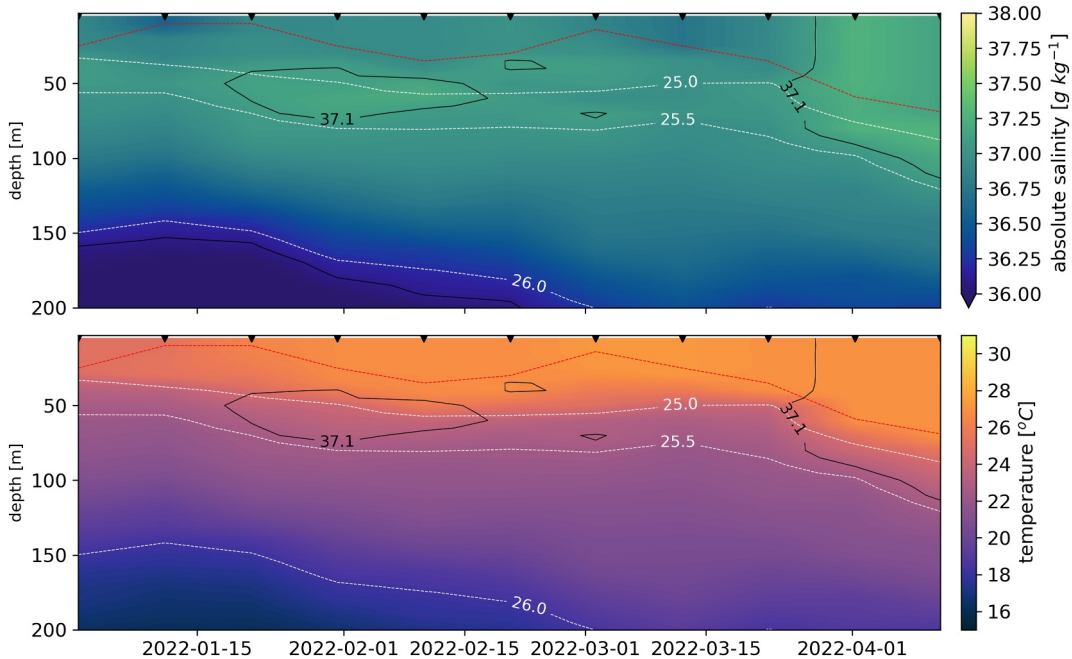


Figure 5. Transects reconstructed from ARGO profiles along line A1 in Figure 1 (WMO ID 3901549), for absolute salinity (top panel) and temperature (bottom panel). The black line indicates the 37.1 g kg^{-1} isohaline, the white isopycnals for 25, 25.5 and 26 kg m^{-3} and red dashed lines indicate the mixed layer depth, using the density criteria. The *x*-axis is time, while the *y*-axis is the depth in *m*. The path of the float is shown from northeast (left) to southwest (right) in Figure 1 as red markers.

averaged geostrophic flow associated with the BC, the CFE, and the eddy dipole than a single-level extraction at 50 m depth would yield.

3.3. Cross-Shelf Connectivity

The previous section presented hydrographic observations made during both cruises, revealing the presence of a S_{max} intrusion (Figure 2). To understand the origin of these structures and their entry mechanisms onto the continental shelf, we investigate the water mass characteristics and their advective velocities in this region using available ARGO profiles, a Glider data set, and altimeter (both gridded fields and tracks) in the weeks leading to and during the cruise. We describe the results using the ARGO observations and Glider data to establish a plausible pathway indicating cross-shelf connectivity in this subsection. Two ARGO floats with paths relevant for our evaluation were selected and displayed by lines A1 (February) and A2 (February–March) in Figure 1.

S_{max} signals present between the open ocean and the shelf edge, obtained from different measurement platforms in the weeks prior to the cruises, illustrate potential connections between these environments (Figures 5 and 6). Two ARGO probes recorded multiple profiles with S_{max} signals that were consistent over time and space. In each ARGO data set, the recorded absolute salinity had values exceeding 37.1 g kg^{-1}, with an increase of approximately 0.3 g kg^{-1} from the surface. These signals were detected at depths ranging from 50 to 75 m, located below the mixed layer and between the 25 and 25.5 kg m^{-3} isopycnals (Figures 5 and 6). The first ARGO (A1) recorded S_{max} between January 20th and February 1st, while during the same period, the second ARGO (A2) did not show any S_{max} signal (Figures 5 and 6). A few days later, the S_{max} signal was observed from February 15th to the end of March, while the ARGO drifted closer to the shelf edge. The similarities between these observations, particularly in the vertical position, indicate that these are the same features. The ARGO tracks suggest this signal moved toward the shelf edge, 50 and 40 days, prior to the S_{max} observation over the shelf (see Figure 8f for map with the location and time of each observation). The southwestward drift of the Argo floats limited the possibility of further analysis.

The Slocum Glider (SG19) sampled this region during March 2022 and enabled the evaluation of the S_{max} advection toward the shelf edge. In this data set, intrusion signals similar to those detected in the Argo floats were observed (Figure 7). To describe the hydrography from the glider (Figure 7), the glider trajectory is divided in

21699291, 2026, 11, Downloaded from https://agupubs.onlinelibrary.wiley.com/doi/10.1029/2025JC023411 by Capes, Wiley Online Library on [10/11/2026]. See the Terms and Conditions (https://onlinelibrary.wiley.com/terms-and-conditions) on Wiley Online Library for rules of use; OA articles are governed by the applicable Creative Commons License

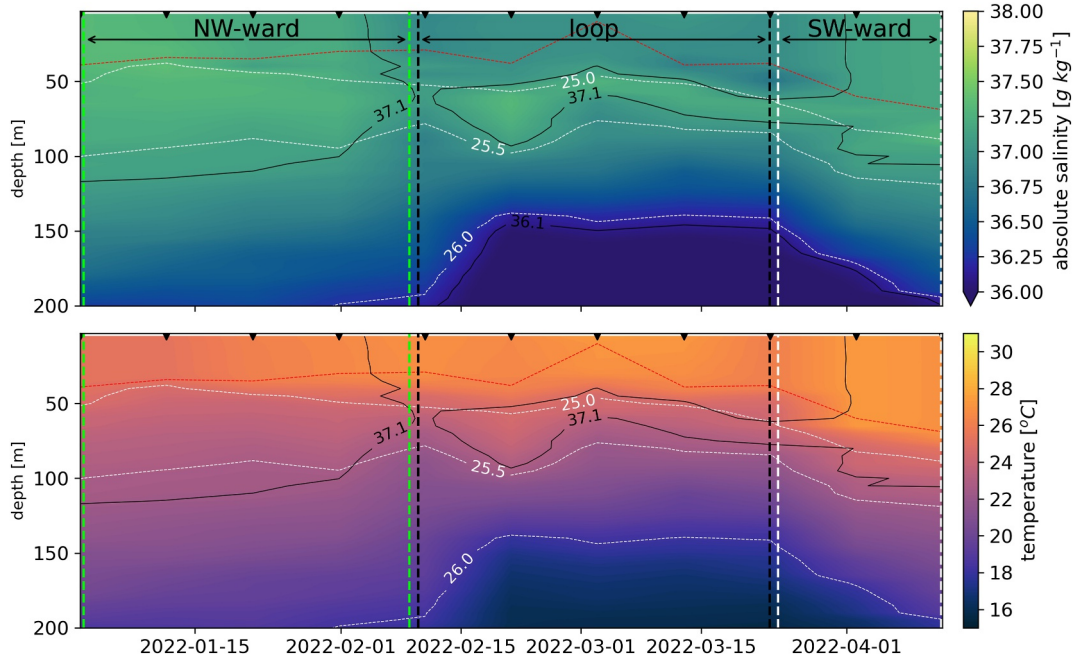


Figure 6. Same as Figure 5, but for ARGO along line A2 in Figure 1 (WMO ID 3901225) and its path from South (left) to North (right) is found in Figure 1 as black markers. The green, black and white vertical dashed lines indicates the periods according to the direction or position of the instrument during its advection (Figure 1).

three segments for analysis: the first extends from March 3rd to 12th and represents the most offshore observations, (Figure 7a), the second is a loop pattern followed by the glider (Figure 7b) from 13th to 19th March, while the last section with data from 22th to 27th March contains the most onshore observations (Figure 7c).

Over the entire period of the first section (Figure 7a), the transect shows the presence of S_{max}, covering an extension of approximately 79 km. After this period, the S_{max} signal is absent when the glider veered toward the shelf edge and to northeast, performing the loop pattern (Figure 7b). When the glider drifted westwards, between days 15 and 20,

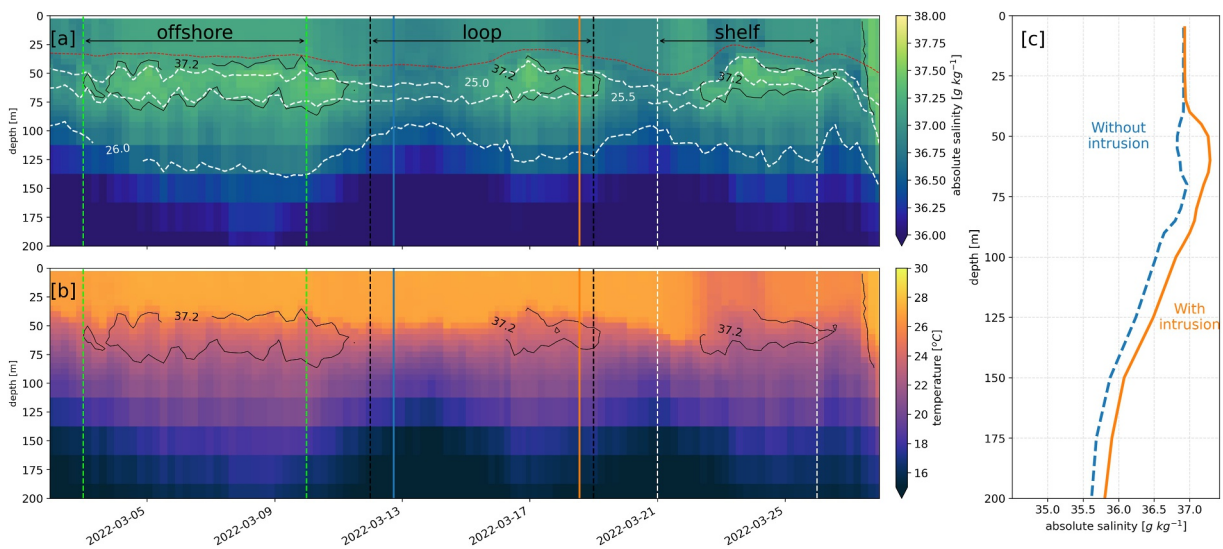


Figure 7. Transects reconstructed from Slocum Glider SG19, for absolute salinity (a) and temperature (b). The black line indicates the 37.2 g kg^{-1} isohaline, the white isopycnals for 25, 25.5 and 26 kg m^{-3} and red dashed lines indicate the mixed layer depth, using the density criteria. The *x*-axis is time, while the *y*-axis is the depth in *m*. The path of the glider is shown in Figure 1 as a continuous black line. The green, black and white vertical dashed lines in (a) and (b) highlights periods where the S_{max} was observed, while the blue and orange continuous vertical lines represents the two profiles in (c), without and with the S_{max} respectively.

21699291, 2026, 11, Downloaded from https://agupubs.onlinelibrary.wiley.com/doi/10.1029/2025JC023411 by Capes, Wiley Online Library on [10/11/2026]. See the Terms and Conditions (https://onlinelibrary.wiley.com/terms-and-conditions) on Wiley Online Library for rules of use; OA articles are governed by the applicable Creative Commons License

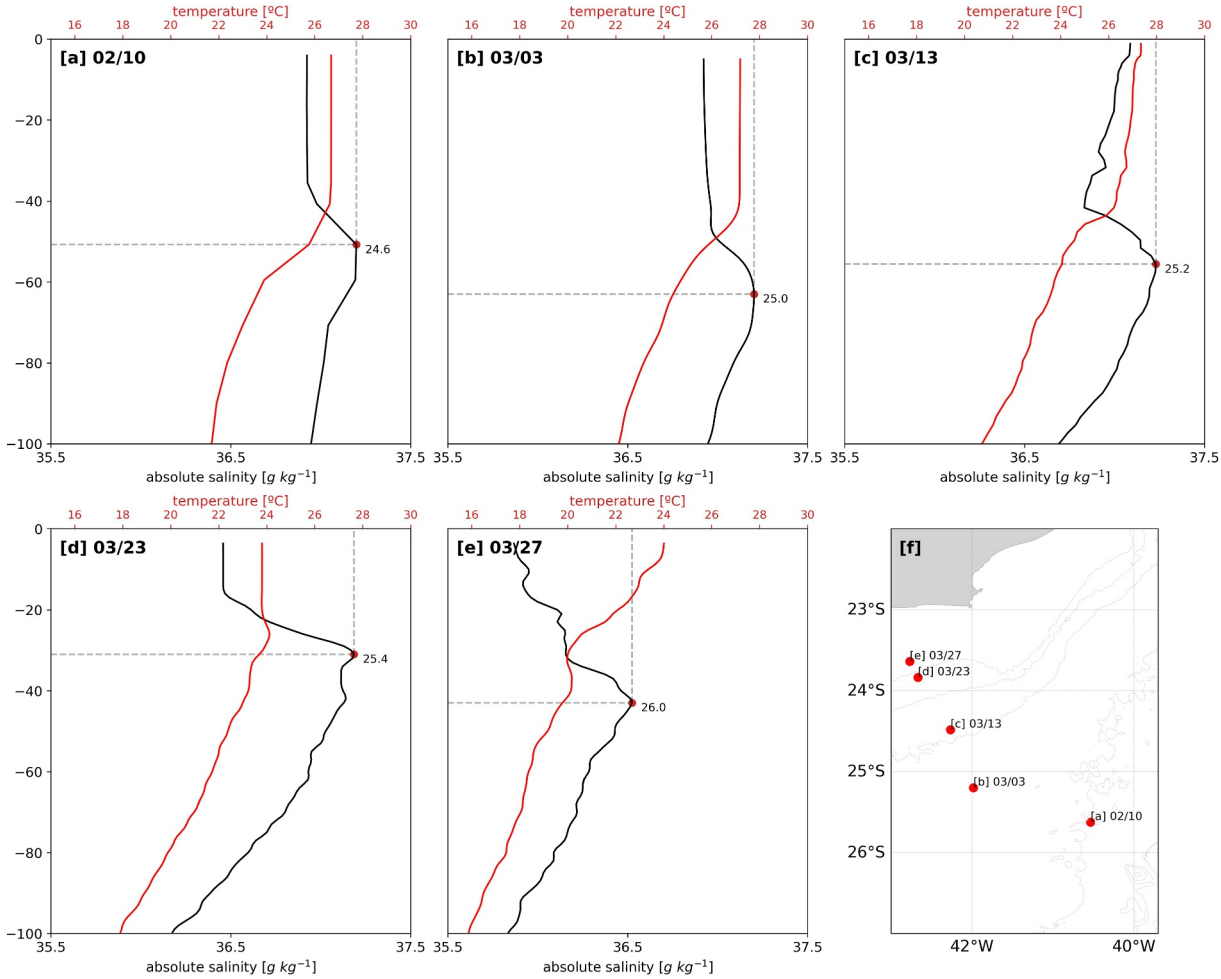


Figure 8. Vertical profiles of absolute salinity (black) and temperature (red) with S_{max} detected by the algorithm used by Silva et al. (2023). Each vertical profile, from a to e, presents the depth of the S_{max} as red marker along its potential density (in kg m^{-3}). In (f) there is the geographical position of each profile, along with their dates for reference. The profiles presented here were selected from the ARGO and CTD data sets (see Section 3.3.1 for more details), as such (f) presents a zoomed subset region.

the salinity maximum was measured once again. The glider sampled almost the same location twice in a 6-day span (Figure 1, zoomed map), hence, it is useful to evaluate the vertical profiles from these dives. For the first profile (Figure 7b, blue) we did not find any intrusion signal, following the S_{max} identification method from (Silva et al., 2023), but 6 days later the S_{max} signal arrived at this location (Figure 7b, orange). The effect of S_{max} increased absolute salinity from 37 g kg^{-1} to 37.4 g kg^{-1}, between 50 and 75 *m* depths, but also had an influence on the water column, increasing the salinity from the MLD to, at least, 200 *m* depth, by about 0.3 g kg^{-1}. The latter portion of the glider data set (Figure 7c) shows once again the S_{max}, this time in closer proximity to the shelf edge.

3.3.1. Water Mass Transformation

In this subsection, we examine the transformation of the S_{max} signal as it is advected from offshore toward the northeastern SBB. The analysis is based on a sequence of hydrographic profiles that document changes in the vertical structure of S_{max}, complemented by the GLORYS12V1 reanalysis to explore its spatial and temporal evolution and to bridge the gaps between in situ observations.

The evaluation of specific vertical profiles from the set of hydrographic data presented allows us to describe the evolution of S_{max} by advection from deep waters to the NE-SBB (Figure 8). Assuming that the same S_{max} was sampled across the data sets, it is possible to track the S_{max} transformation with time and relate these changes to the main hydrodynamical processes in this region, like wind or eddy-driven circulation (Calado et al., 2010; Rocha & Simoes-Sousa, 2022; Silveira et al., 2023; Uchoa et al., 2023). Figure 8 shows the consecutive locations

21699291, 2026, 11, Downloaded from https://agupubs.onlinelibrary.wiley.com/doi/10.1029/2025JC023411 by Capes, Wiley Online Library on [10/11/2026]. See the Terms and Conditions (https://onlinelibrary.wiley.com/terms-and-conditions) on Wiley Online Library for rules of use; OA articles are governed by the applicable Creative Commons License

21699291, 2026, 11, Downloaded from https://agupubs.onlinelibrary.wiley.com/doi/10.1029/2025JC023411 by Capes, Wiley Online Library on [10/11/2026]. See the Terms and Conditions (https://onlinelibrary.wiley.com/terms-and-conditions) on Wiley Online Library for rules of use; OA articles are governed by the applicable Creative Commons License

of profiles that have been traced chronologically to follow the advection of the salinity maximum intrusion from offshore to the shelf region of SBB.

In terms of water mass change throughout the profiles (Figures 8a–8d), the S_{max} presented salinity higher than 37 g kg^{-1}, associated with the presence of TW at the mixed layer, which is a salty and warm water mass (S $\geq$ 37 g kg^{-1} and $T \geq 24$°C, Cerda & Castro, 2014), characteristic of the southwestern South Atlantic (Castro & Miranda, 1998). Note that the temperature in the first three profiles (Figures 8a–8c) also shows warmer conditions, which have relevant impacts over the S_{max} density. The salinity reduces to 36.5 g kg^{-1} and temperature decreases in about 4°C once over the shelf (Figures 8d and 8e). The drop in salinity can be related to the mixing with SACW, characterized by the relatively colder waters (colder than 18^{o}C, Cerda & Castro, 2014). This is possible under upwelling favorable wind conditions, in which SACW is uplifted or upwelled, decreasing the temperature and salinity at the surface levels (Castro & Miranda, 1998; Cerda & Castro, 2014). The amount of information is limited and does not allow us to infer the changes between the first and the second profiles. However, these hydrographic conditions reveal the influence of local processes in the vertical position S_{max} and the density associated with the maximum salinity.

To overcome the gap between profiles, we investigated the salinity and horizontal velocity patterns at a 50-m depth layer from GLORYS12V1, along with the geostrophic currents derived from altimetry, to understand the advection of S_{max} toward the shelf (Figure 9). On February 4, a salinity maximum ($S > 37$ psu) is observed offshore the NE-SBB, reaching a close proximity with the location of the first ARGO profile on February 10 (Figure 9a). The geostrophic currents indicate a southwestward flow, consistent with the ARGO float trajectory, revealing a S_{max} moving southwards, reaching the southernmost point on February 18 (Figure 9b) from where it starts to move shoreward. On March 3, this feature is located slightly to the west of the second observation from ARGO (Figure 9c). From March 6 to 27, the S_{max} is advected toward the shelf, describing a movement similar to what was observed from the CTD profiles, although slightly westward. The geostrophic currents during this period show the development of an eddy dipole, pushing the S_{max} signal shoreward and becomes fully developed on March 27, date where we last observed the feature (Figure 9d and Figure 4c). The full advection of S_{max} from offshore to the shelf takes approximately 50 days, consistent with the time interval between the first ARGO observation and the CTD profiles. After that, the tracking is no longer possible due to shelf processes that either dissipate the S_{max} or mix it with fresher waters. The Movie S1 shows the full temporal evolution of the salinity field at 50 m depth, along with the horizontal velocity at the same depth. To assure the vertical structure of these signals represent a S_{max}, we selected GLORYS12V1 profiles from specific locations tracking the S_{max} signal (Figure S2 of Supporting Information S1), and comparing them with the in situ measurements (Figure 9). Despite a slight westward displacement, the GLORYS12V1 profiles reproduce the main vertical structure and hydrographic features observed in the in situ profiles (Figures S2a–S2g of Supporting Information S1), indicating a reasonable consistency between the reanalysis and observations.

To assess the reliability of GLORYS12V1 for this region, we compared reanalysis profiles of absolute salinity and temperature against in situ observations at five locations along the chronological S_{max} sequence (Figures S3 and S4 of Supporting Information S1) and against Slocum Glider profiles (Figure S5 of Supporting Information S1). GLORYS12V1 reproduces the main vertical structure and hydrographic characteristics observed in situ, but salinity is systematically overestimated and the amplitude of the S_{max} signal is underestimated relative to in situ measurements (Figure S3 of Supporting Information S1). Temperature is better represented in the upper 20 m, consistent with GLORYS12V1 assimilating satellite-derived data. Biases increase toward the shelf for both variables, suggesting that shelf processes are not fully resolved in the reanalysis. Quantitatively, the RMSE against the Slocum Glider data set is smaller at the surface (1.18^{o}C) and increases with depth (2.24^{o}C at 100-m depth) for temperature. In contrast, the salinity difference is almost the same throughout the water column (0.38 near the surface and 0.39 g kg^{-1} at 100-m depth).

3.4. Lagrangian Pathways

A set of Lagrangian experiments were used to investigate potential pathways and sources of the observed S_{max} intrusions toward the NE-SBB shelf. Four experiments were run based on previous analysis (see Section 3.3.1 and Movie S1): two back-propagation experiments releasing particles at 50 m (BPI) and along the 25.5 kg m^{-3} isopycnal (BPII), and two forward experiments releasing particles north (FPN) and east (FPE) of the region of interest, at 50 m depth for both. The experiments BPI, FPN, and FPE used the full three-dimensional

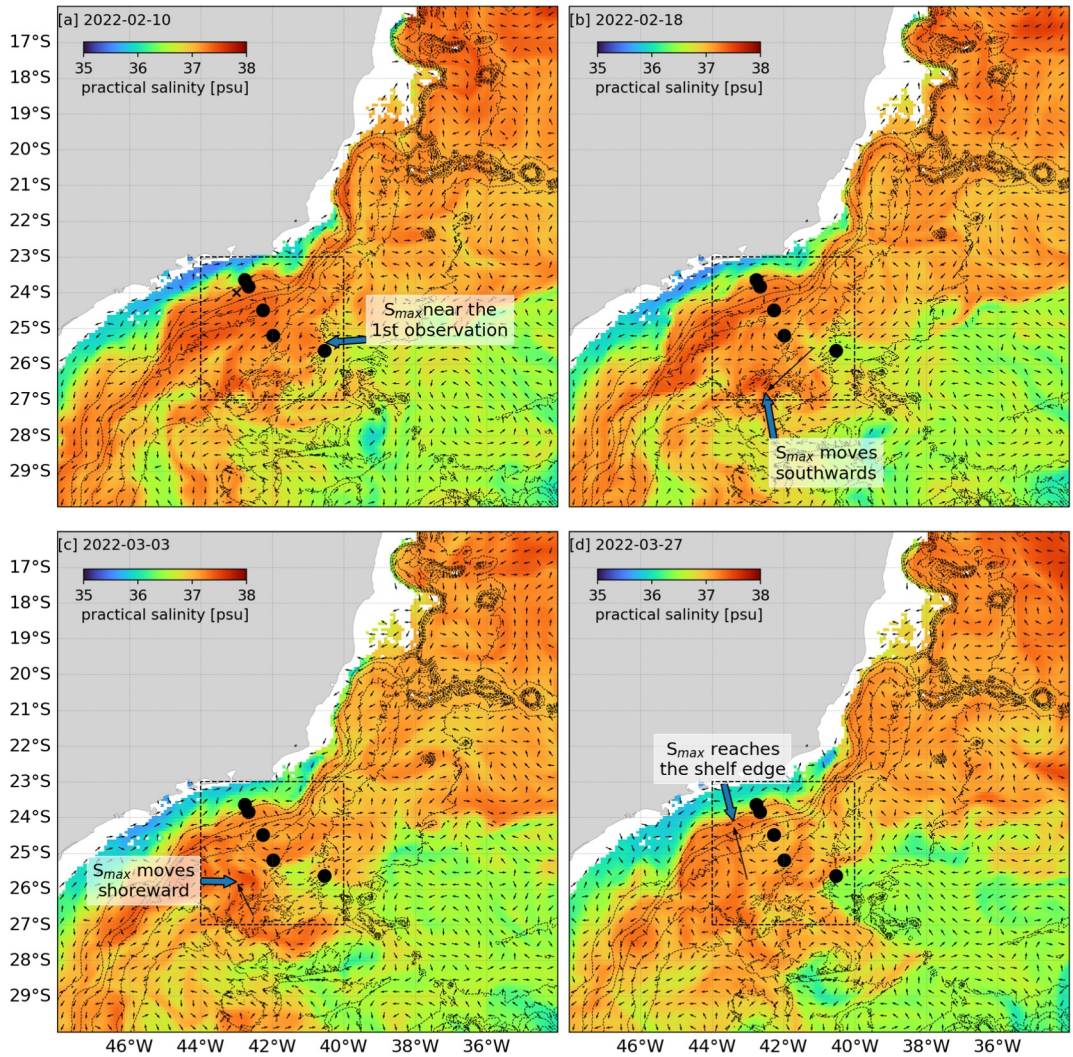


Figure 9. Snapshots of the S_{max} advection on the GLORYS12V1 data set, with practical salinity (in psu) at 50 m depth in colors and horizontal velocity in black arrows at the same layer, for (a) February 10, (b) February 18, (c) March 3 and (d) March 27 of 2022. Bathymetry from GEBCO2019 (Weatherall et al., 2015) is represented by thin gray lines. The black dashed box represents the region of interest, to highlight the advection throughout the period. The black dots in each panel represent the selected vertical profiles presented in Figure 8. The entire advection is found in the Movie S1.

GLORYS12V1 velocity field at 50-m depth level, while for the experiment BPII GLORYS12V1 velocities were interpolated onto the 25.5 kg m^{-3} isopycnal layer to constrain advection to this density layer. All experiments were seeded with 100 particles within a 1-degree by 1-degree box around a launch point. For the two backtracking experiments, the launch point was at 42.77^{o}W and 23.64^{o}S on March 27, matching the last observation of S_{max}. The release points for the northern and eastern forward propagation experiments were chosen at 40^{o}W, 22^{o}S and 38^{o}W, 26.5^{o}S, respectively, approximately 40 days prior to the last observation on the shelf. Table 2 summarizes the Lagrangian experiment setups.

The backtracking experiments reveal two potential pathways for S_{max}: (a) cross-shelf components that can be advected westward either through a meandering pathways offshore of NE-SBB or (b) via along-shelf advection over the 200 m isobath, originating from the north, both occurring within approximately 40 days (Figure 10a). The cross-shelf pathway represents the highest probability, accounting for 30% of the particles seeded on the shelf (BPI, Figure 10a). It presents a meandering shape, possibly around a set of cyclonic and anticyclonic eddies, swirling along the shelf toward the shelf edge while effectively transporting particles across the shelf. There is a particle hotspot centered at 42^{o}W and 25^{o}S, where they do not present a clear pathway but instead show an

21699291, 2026, 11, Downloaded from https://agupubs.onlinelibrary.wiley.com/doi/10.1029/2025JC023411 by Capes, Wiley Online Library on [10/11/2026]. See the Terms and Conditions (https://onlinelibrary.wiley.com/terms-and-conditions) on Wiley Online Library for rules of use; OA articles are governed by the applicable Creative Commons License

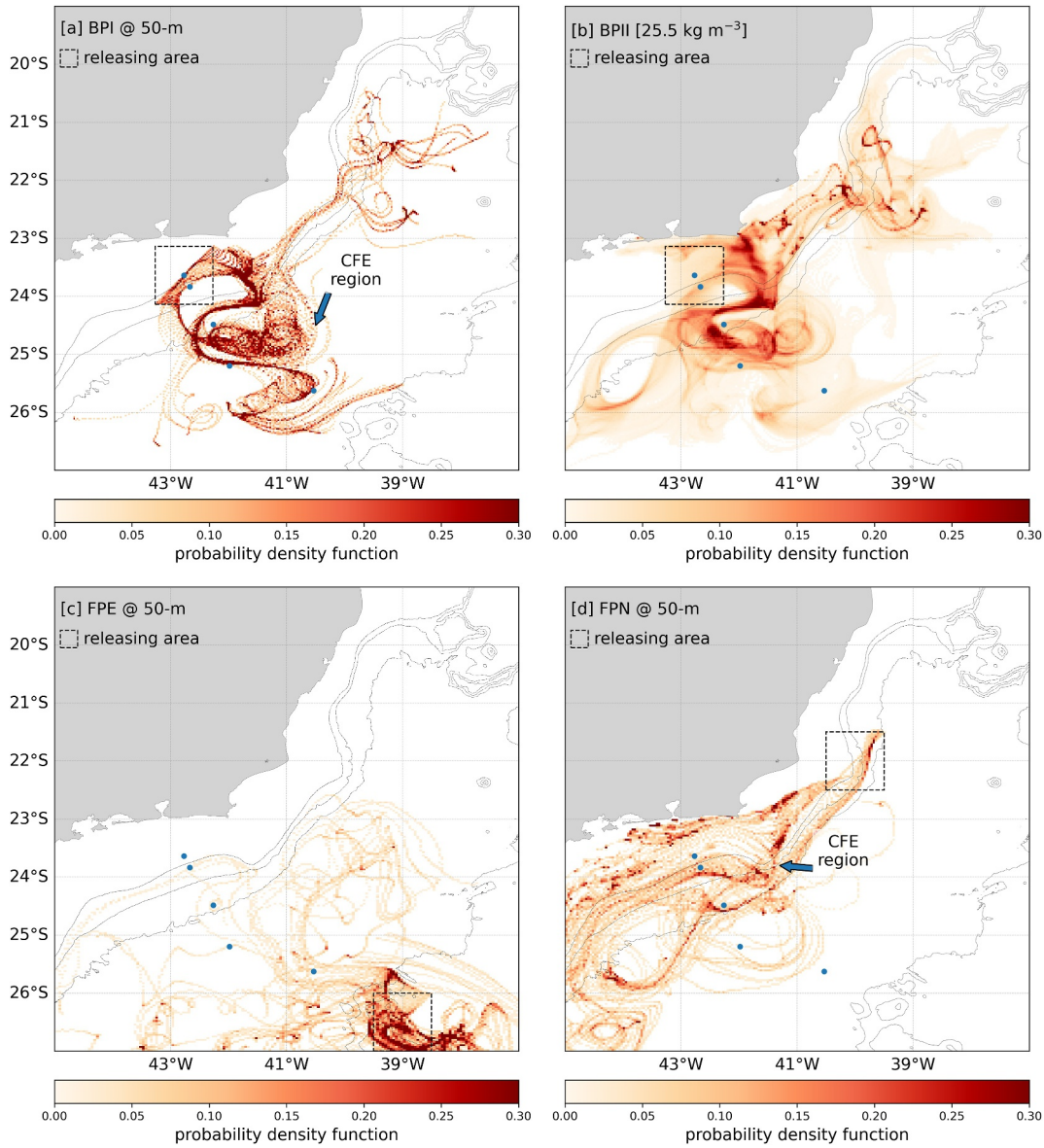


Figure 10. Time and vertically integrated particles concentration on (a) the 3D GLORYS12V1 and (b) the isopycnal surface velocities backpropagation experiments with release at the last S_{max} observed on 27th March over the shelf at 50-m depth. Panels (c) and (d) are for the forward propagation experiments (FPE and FPN, respectively). The red markers in all subpanels indicates the location of the sequence of profiles from Figure 8. The black dashed box on each panel represent the seeding location, better described in Table 2. Note that the smoother appearance in panel b reflects its isopycnal-based extraction, whereas panels (a, c, and d) sample fixed geopotential layers, causing particles to scatter across depth bins and producing a noisier pattern.

accumulation, although a main path is still distinguishable. After 40 days, particles were mostly backtracked to offshore regions off the seeding location. This Lagrangian analysis result provides a better fit with the selected vertical profiles used to understand the transformation of the water mass (Figure 8), as indicated by the red dots in Figure 10a. Comparatively, the BPII experiment (Figure 10b) shows similar results to the previous experiment (BPI). It is noteworthy that in BPII, more particles were advected over the shelf between Cabo de São Tomé and Guanabara Bay (Figure 1), unlike in the previous experiment. Combined, BPI and BPII analysis show the cross-shelf and the along-shelf are both reasonable candidates as origins of the S_{max} on the continental shelf.

Although the eastern source appears to be the most probable origin of March 2022 S_{max}, as indicated by the cross-shelf pathway, a secondary source was identified via backpropagation analysis. The along-isobath pathway brings

21699291, 2026, 11, Downloaded from https://agupubs.onlinelibrary.wiley.com/doi/10.1029/2025JC023411 by Capes, Wiley Online Library on [10/11/2026]. See the Terms and Conditions (https://onlinelibrary.wiley.com/terms-and-conditions) on Wiley Online Library for rules of use; OA articles are governed by the applicable Creative Commons License

21699291, 2026, 11, Downloaded from https://agupubs.onlinelibrary.wiley.com/doi/10.1029/2025JC023411 by Capes, Wiley Online Library on [10/11/2026]. See the Terms and Conditions (https://onlinelibrary.wiley.com/terms-and-conditions) on Wiley Online Library for rules of use; OA articles are governed by the applicable Creative Commons License

particles from a northern location of the region of interest (Figure 10a), transporting particles following the isobaths. However, off Cabo Frio, both pathways merge, making it not possible to separate one from another.

To better understand the relative contribution of each pathway, two forward propagation experiments were conducted (FPE and FPN). Results indicate that particles released from east (FPE, Figure 10c) did not reach the shelf area. In contrast, particles released from the north (FPN, Figure 10d) successfully reached the shelf region within the 40-day timeframe, following an alongshelf pathway with meanders leading a cross-shelf secondary pathway. A four-segment pathway seems to be a suggestive advection route for the salinity intrusion in the FPN which include: (a) the BC meandering southwestward from the source region; (b) around the CFE–aided by the eddy to go around toward the shelfbreak; (c) probably enhanced by a proximate anticyclonic eddy to the west of the CFE; (d) aided by the meandering BC around the CFE as well, finally reaching the shelfbreak. Note that although the SBB is often classified as a wider shelf with direct influence from the BC at the edge (Zembruscki, 1979), the NE-SBB compartment is narrower with a stronger influence of the BC (Castro, 2014; Castro & Miranda, 1998; Dottori et al., 2023; Zembruscki, 1979). This suggested pathway is somewhat similar to the BC pathway shown for another cruise in 2001 analyzed by Calado et al. (2006) (see their Figure 1) for parameterizing the CFE.

Using results from FPN, the only experiment that reached the region of interest, we have found that 31% of the particles that reached the shelf area did so within 10-day, covering a cumulative distance of 335 km and under the influence of high EKE during 26% of that time. In contrast, 21% of the particles reached the shelf area after 20 days on average, with a cumulative distance covered of 541 km, spending 37% of this time under high EKE activity, which is signicantly higher than the first case (Mann-Whitney Test, p-value < 0.001). Additional details on the Lagrangian experiments are provided in Text S1 and Figure S7 of Supporting Information S1.

We acknowledge the discrepancies between back and forward propagation, due to initial conditions sensitivity and biases errors on Lagrangian analysis (Reijnders et al., 2026). However, the spatial convergence of particles over the region of interest on both back and forward propagation experiments, combined with the location where $S_{\max}$ were found and the GLORYS12V1 analysis, indicates a preference for northern sources.

3.5. Ekman Transport on the Shelf

The surface Ekman transport (T_{Ek}), calculated from wind stress, is presented in Figure 3 as vectors. It shows that throughout the first observational cruise, T_{Ek} was predominantly toward offshelf (Figure 3d), due to constant northeasterly winds, from the South Atlantic Subtropical High (SASH, Stech, 1990), generating an offshelf Ekman Transport of approximately 80 $m^2\ s^{-1}$. Winds from SASH has an average intensity of 10 $m\ s^{-1}$ (Pimenta et al., 2019), with a lower frequency of cold fronts (Stech, 1990), its persistence drives significant cross-shelf exchanges, pushing water offshore and by mass conservation cold and nutrient rich waters (SACW) upwells or uplift nearshore. It results in coastal upwelling such as the one observed during the first transect, which also generates a cross-shelf SST gradient (Figure 3a). Between both samplings, the wind patterns changed and intensified, associated with a cold front passage that inverted the wind direction (Stech, 1990). Not only did it affect the sea surface by changing the input of momentum, but also the incident solar radiation due to an increase in cloud coverage, which subsequently reduced the SST (Figure 3b). The wind inversion was not persistent enough to generate an onshelf surface T_{Ek} (not shown), resulting only in relatively weaker offshelf T_{Ek}, reducing from 50 $m^3\ s^{-1}$ between cruises (Figures 3e) to 20 $m^3\ s^{-1}$ in the second cruise (Figure 3f).

Onshore transport occurs at depth in response to offshore Ekman transport at the surface, either near the bottom or in midwater (Lentz & Chapman, 2004). During the analyzed period, the onshelf transport over the shelf edge was expected to be above the bottom Ekman layer, that is, in subsurface levels, as given by the slope Burger number (Bu) higher than 1 (Lentz & Chapman, 2004) as presented in Table 3.

4. Discussion

4.1. Observational Evidence and Broader Context of $S_{\max}$ Intrusions

The hydrographic observations off the northeastern SBB (NE-SBB) reveal recurrent mid-depth salinity maxima ($S_{\max}$) detected at multiple locations and times during March 2022. The spatial and temporal coherence of these features, together with the remarkable consistency of their vertical structure despite offsets among individual

Table 3
Summary of Topographic Gradient (α), Buoyancy Frequency (N^2) and Burger Number (Bu, Equation 5) Computed for Specific CTD Profiles Extracted From SANAGU14 and SANAGU15 Campaings

Vertical profile	α	$N^2[s^{-1}]$	*Bu*
G4	23×10^{-3}	5.96×10^{-5}	9.15
G4′	23×10^{-3}	4.65×10^{-5}	7.14
H4	11×10^{-3}	5.32×10^{-5}	2.16

Note. The location of both profiles are represented in Figure 1 as black stars. α and *Bu* are dimensionless numbers.

profiles, indicates that the observed S_{max} intrusions correspond to the same advective feature sampled at different stages of its evolution, rather than to locally generated anomalies. The intrusions are characterized by well-defined subsurface salinity maxima occupying mid-depth layers, consistent with previous hydrographic surveys in the region (Silva et al., 2023), supporting an essentially advective origin for the S_{max} signal.

The characteristics of the mid-depth S_{max} intrusions observed in the NE-SBB are also similar to those reported on other continental shelves, most notably in the MAB, as well as in previous surveys in the SBB (Campos et al., 2000; Castro, 2014; Silva et al., 2023). In these regions, S_{max} intrusions are associated with subsurface salinity maxima typically found at mid-depths, with vertical thicknesses on the order of 20–30 m, and are more frequently observed during summer conditions (Lentz, 2003). This similarity suggests that S_{max} intrusions represent a recurrent feature of stratified continental shelves.

Previous studies indicate that the formation and persistence of S_{max} intrusions involve a combination of lateral advection and double-diffusive processes (Gawarkiewicz et al., 2022, 2025; Lentz, 2003; Silva et al., 2023). In the MAB, the increasing frequency and enhanced shelfward penetration of S_{max} intrusions since the early 2000s have been linked to a rise in warm-core ring activity, with anticyclonic mesoscale eddies playing a central role in their formation and delivery to the shelf (Gangopadhyay et al., 2019; Silver et al., 2023). In the SBB, cyclonic mesoscale features, such as the CFE, are the possible mechanism promoting S_{max} intrusions onto the shelf, similarly to the offshore waters injection onto the shelf on the Australian shelf (Malan et al., 2020) and MAB (Gawarkiewicz et al., 2025).

4.2. Mesoscale Role on the S_{max} Advection

Both backward and forward propagation Lagrangian highlight the role of the CFE as a conduit for advecting S_{max} from offshore toward the shelf edge. Subsequently, these S_{max}-intruded waters on the southwestern edges of the CFE are carried by cross-shelf wind-driven currents to inject these features onto the shelf. Regarding the upstream source, the backpropagation suggests an eastern origin, in contrast to the forward propagation experiments combined with GLORYS12V1, which points to the north. This discrepancy might be attributed to the initial condition sensitivity and known biases in the backward propagating Lagrangian analysis (Reijnders et al., 2026). The northern origin seems to be the preferred source of origin of S_{max} (possible pathways are mentioned below), which is also independently supported by recent high-resolution numerical (5 km) simulations of the SBB circulation, where S_{max} is advected from the north (Silva, 2024) and reaches the shelf around CFE. Further longer term backward propagation experiments and high-resolution simulations will be required to definitively address the source/origin issue of the offshore S_{max}.

The S_{max} could possibly reach the NE-SBB shelf through two pathways from the northern source regions that resemble the dynamics of the BC. An alongshelf pathway, flowing southwestwards along the shelf edge, resembles a nonmeandering configuration of the BC (Da Silveira et al., 2008), transporting S_{max} directly from their source right onto the NE-SBB shelf. The second pathway describes a cross-shelf route driven by the abrupt change of coastline orientation, where the BC continues flowing southwards by inertia but turns to the shelf due to potential vorticity conservation, developing the BC meander at this latitude (Da Silveira et al., 2008; Mascarenhas et al., 1971). This meander often releases from the BC and generates the CFE due to baroclinic instability (Da Silveira et al., 2008; Luko et al., 2022; Rocha & Simoes-Sousa, 2022; Silveira et al., 2023; Uchoa et al., 2023). Consistent with this interpretation, the observational data set shows that all S_{max} intrusions occur below the mixed layer, where the influence of high-frequency atmospheric forcing is weak (Giunta & Ward, 2022). This vertical

21699291, 2026, 11, Downloaded from https://agupubs.onlinelibrary.wiley.com/doi/10.1029/2025JC023411 by Capes, Wiley Online Library on [10/11/2026]. See the Terms and Conditions (https://onlinelibrary.wiley.com/terms-and-conditions) on Wiley Online Library for rules of use; OA articles are governed by the applicable Creative Commons License

21699291, 2026, 11, Downloaded from https://agupubs.onlinelibrary.wiley.com/doi/10.1029/2025JC023411 by Capes, Wiley Online Library on [10/11/2026]. See the Terms and Conditions (https://onlinelibrary.wiley.com/terms-and-conditions) on Wiley Online Library for rules of use; OA articles are governed by the applicable Creative Commons License

structure reinforces the role of mesoscale dynamics in governing the advection of the S_{max} signal toward the shelf edge.

The hydrographic data set only provides a snapshot of a longer and more complex advective conditions. These results imply that multiple advective pathways contributes to the supply of S_{max} for the NE-SBB, with their relative importance modulated by the regional circulation conditions. Approximately 50% of the particles released at a northern location reach the NE-SBB, either by an alongshelf pathway (31%) or by a longer cross-shelf route (21%). The comparable contributions of these pathways are noteworthy, as cross-shelf transport would be expected to be more intermittent given the episodic nature of eddy formation. However, the CFE is a quasi-stationary feature, characterized by a mean lifetime of approximately 71 days and a formation rate of about 3.5 events per year (da Silveira et al., 2023), which suggests that its role in facilitating cross-shelf advection is significant and episodic rather than negligible.

4.3. Mechanisms Driving Onshelf S_{max} Intrusions

Throughout its advection, the S_{max} signal is subject to various physical processes that influence its transport and distribution, including directing the advection toward the shelf instead of alongshelf as one would expect considering the BC main flow. The interaction between the BC and the cyclonic CFE appears to be the main process in the advection of S_{max} toward the shelf edge. While flowing around the CFE, the BC branches may experience different normal acceleration due to the curvature of the flow: the shoreward branch will have a smaller curvature compared to the offshore branch, therefore, affecting the acceleration (by doubling the radii of the curvature reduces the acceleration in half), which can lead to the shoreward branch hitting the shelf edge perpendicularly and vanishing, while other branches continue flowing alongshelf. This mechanism can effectively redirect the S_{max} signal toward the shelf edge, as supported by the forward particle tracking experiments, showing that particles from north, a possible source of S_{max}, are advected toward the shelf break along the CFE edges. Moreover, the eddy dipole formation between the CFE and an anticyclonic eddy southwest of it can intensify even more the cross-shelf transport of S_{max} toward the shelf break, similarly to mid-depth intrusions found in the MAB (Gawarkiewicz et al., 2025) and Australia (Malan et al., 2020), possibly injecting S_{max} fruther onshore.

Once S_{max} is delivered to the shelf edge by mesoscale advection, its penetration onto the continental shelf requires ageostrophic cross-shelf processes (Brink, 2016; K. Chen et al., 2022). In the northeastern SBB (NE-SBB), shoreward wind-driven cross-shelf exchanges have been found in numerical experiments between 50 and 100 m depth (Combes et al., 2021), under northeasterly wind conditions (upwelling favorable), such as those observed during the study period. The slope Burger number (Bu; Table 3) supports this interpretation, where values greater than one indicate a mid-depth Ekman-driven counterflow (Lentz & Chapman, 2004), consistent with the locations where S_{max} was found within the shelf. While wind-driven processes enable the cross-shelf injection of S_{max}, the background stratification ultimately controls its vertical confinement within the shelf. The enhanced summer stratification found in the NE-SBB promotes relatively shallow and thin intrusions, due to the presence of the South Atlantic Central Waters (SACW) below the S_{max} intrusion, which limits downward penetration of the S_{max} signal (Silva et al., 2023). It is interesting to note that, differently from the SBB, the MAB S_{max} are not wind-driven (Lentz, 2003). That is likely due to the shelf width difference, where MAB is wider (approximately 100–120 km) than NE-SBB (between 50 and 60 km, Castro, 2014).

The March 2022 observations documented here are representative of a significant recurrent process in the NE-SBB. The climatological inventory of Silva et al. (2023), built from 35 years and approximately 2160 vertical profiles, identified S_{max} intrusions in 27% of all profiles with no statistically significant seasonal variability in occurrence frequency, establishing these features as a year-round characteristic of the region rather than an isolated event. Within our own data set, S_{max} signal were detected across different instruments from January through March 2022, collectively pointing to continuous supply from the north. The importance of the delivery mechanism is further supported by the quasi-stationary nature of the CFE, with a mean lifetime of approximately 71 days and a formation rate of about 3.5 events per year (Silveira et al., 2023), and by the independent documentation of the same BC–CFE pathway during a 2001 cruise (Calado et al., 2006).

The onshelf injection is likely subject to seasonal modulation, as the Burger number is sensitive to stratification, which varies seasonally in the SBB (Castro, 2014; Silveira et al., 2023). The strong summer stratification observed in March 2022 yields Bu $\gg$ 1, confining the compensating onshore flow to the mid-water column and

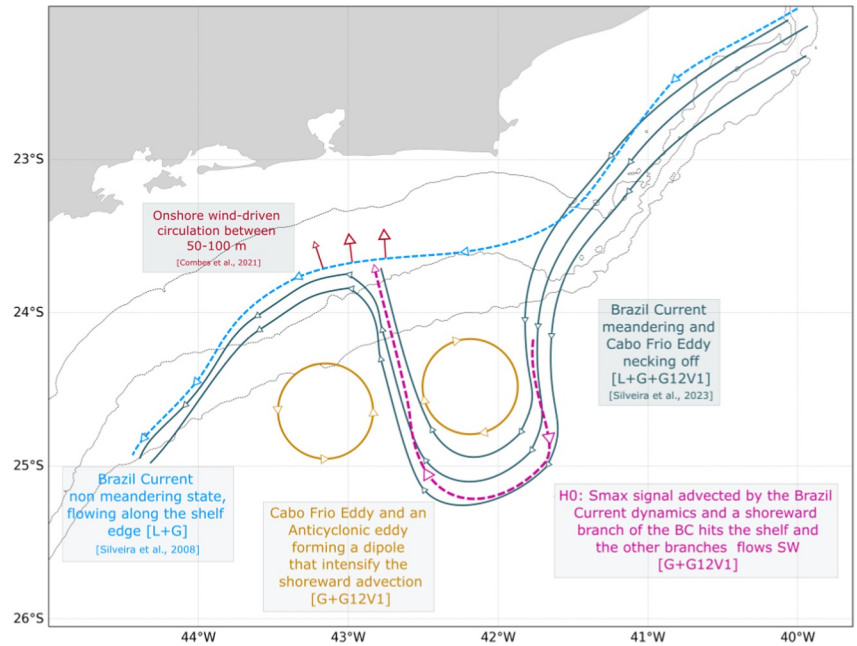


Figure 11. Schematic flow field zoomed at the main area of interest, summarizing the main processes advecting Salinity Maximum (S_{max}) signals, obtained from the jointly analysis of the geostrophic fields (G, Figure 4), Lagrangian outputs (L, Figure 10), and GLORYS12V1 analysis (G12V1, Figure 9). S_{max} are transported from north by the Brazil Current dynamics (dark and light blue), the pathway is influenced by the Cabo Frio Eddy presence (color), which also form an eddy dipole intensifing the S_{max} advection toward the shelf break (pink colors). Finally, at the shelf edge, wind-driven circulation is responsible to transport these S_{max} signals onto the shelf, becoming S_{max} intrusions (dark red arrows).

producing the shallow (25–50 m) intrusion depths reported here (Figure 2). In winter, reduced stratification lowers Bu toward 1, shifting the compensating flow toward the bottom boundary layer (Lentz & Chapman, 2004) and producing deeper (median $ZS_{max} = 33$ m) and thicker (median $\delta = 35$ m) intrusions (Silva et al., 2023) at the same shelf compartment. Additionally, cold-front passages in winter temporarily reverse the prevailing north-easterly winds, driving surface onshore Ekman transport that pushes TW inshore at shallow levels (Campos et al., 2000; Castro, 2014), providing an alternative injection pathway during the colder season. Together, these processes suggest why S_{max} occurrence frequency is roughly constant year-round while the intrusion depth, thickness, and salinity anomaly exhibit significant seasonal differences.

Our results suggest that mesoscale dynamics advect the S_{max} signal from remote locations to the shelf edge, and that wind and stratification together inject it into the shelf, thereby developing a S_{max} intrusion (summarized on Figure 11). Despite the consistency between observations, reanalysis, and Lagrangian results, this study has limitations that should be acknowledged. Our hydrographic data set provides only a snapshot of the complex and dynamic processes governing S_{max} intrusions in the NE-SBB and does not resolve their temporal variability. The Lagrangian experiments, while informative, are based on reanalysis data that may not fully capture the fine-scale dynamics of the region, particularly during strong mesoscale activity. Additionally, the assumption of passive particle advection neglects potential mixing and diffusion processes that could influence the transport and transformation of S_{max}. High-resolution numerical simulations designed to isolate the processes are required to quantify interactions among the mechanisms discussed here under different forcing regimes (e.g., Brink, 2026; H. Chen et al., 2019; Palóczy et al., 2016; Wang & Jordi, 2011).

5. Concluding Remarks

In this study, we present the first observational evidence of remotely advected mid-depth Salinity Maximum (S_{max}) intrusions in the Northeastern South Brazil Bight (NE-SBB). Using a multi-platform observational data set, we tracked the pathway of S_{max} from eastern locations off the NE-SBB to the continental shelf in this region. Our

21699291, 2026, 11, Downloaded from https://agupubs.onlinelibrary.wiley.com/doi/10.1029/2025JC023411 by Capes, Wiley Online Library on [10/11/2026]. See the Terms and Conditions (https://onlinelibrary.wiley.com/terms-and-conditions) on Wiley Online Library for rules of use; OA articles are governed by the applicable Creative Commons License

findings indicate that oceanic S_{max} is consistent with those observed over the shelf (Silva et al., 2023), characterized by waters saltier than 37 $g\ kg^{-1}$ and occurring between 50 and 100 m depth. Backpropagation Lagrangian results indicate the origin of S_{max} being northeast of the study region.

A key result in this study identifies the BC and the CFE interaction as the main mechanism advecting S_{max} toward the shelf, describing a cross-shelf pathway. Once at the shelf break, Ekman transport associated with upwelling-favorable winds act as the main process pushing S_{max} further onto the shelf. In addition to the cross-shelf pathway, our analysis found two secondary processes: (a) the enhancement of the cross-shelf advection process by the interaction between the CFE and an anticyclonic eddy, forming an eddy dipole, and (b) a southwestward alongshelf pathway, resembling a non-meandering BC regime, advecting S_{max} directly from their source.

Our results shed light on the origins and pathways of S_{max}, a poorly understood phenomenon in the SBB. Recognizing these intrusions of warm, salty waters is essential for advancing our understanding of the Cabo Frio upwelling system. Moreover, under climate change scenarios, further studies in the NE-SBB are required to evaluate how S_{max} dynamics may influence the thermodynamics of the continental shelf.

Conflict of Interest

The authors declare no conflicts of interest relevant to this study.

Availability Statement

The CTD casts from the SANAGU research cruises (Moreira et al., 2023), belong to Petrobras and are not accessible to the public or research community. The ARGO profiles were obtained on April 2023 from the Institu Français de Recherche pour l'Explotation de la Mer (IFREMER), via ARGOPY package (Maze & Balem, 2020). The Slocum Glider SG19 data set is not accessible to the public or research community, but it is possible to request access through ProjetoAzul at http://www.projetoazul.eco.br/ (Alves dos Santos et al., 2015). GLORYS12V1 data is available from EU Copernicus Marine Service at https://doi.org/10.48670/moi-00016 (Jean-Michel et al., 2021). ERA5 output is available from the Copernicus Climate Change Service at https://doi.org/10.24381/cds.adbb2d47 (Hersbach et al., 2018). The bathymetry data were downloaded from GEBCO 2019; Weatherall et al., 2015). The altimeter data set and derivative products from them were processed by SSALTO/DUACS and distributed by CMEMS (CMEMS, 2024a; CMEMS, 2024b) with support from the Centre national d'études spatiales (CNES). The precipitation data set from MERGE were obtained on April 2023, from the National Institute on Spatial Research (or INPE in Brazilian Portuguese) website (https://ftp.cptec.inpe.br/modelos/tempo/MERGE/GPM/DAILY/). The sea surface temperature were obtained from the National Centers for Environmental Information (NCEI), via their website (https://www.ncei.noaa.gov/data/oceans/pathfinder/Version5.3/L3C/). This work used the Gibbs-Seawater Oceanographic Toolbox with the python package GSW (McDougall & Barker, 2011), CTD data were processed with Python-CTD (Fernandes, 2014), multi-dimensional data were handled using Xarray (Hoyer & Hamman, 2017), data analysis were performed with NumPy (Harris et al., 2020) and data visualization was made with Matplotlib (Hunter, 2007). All scripts used to reproduce the figures and analysis in this manuscript are available at https://doi.org/10.5281/zenodo.12735814.

Acknowledgments
We thank Petróleo Brasileiro S.A. (PETROBRAS) for their permission to use and display the proprietary data from Santos Project–Santos Basin Environmental Characterization–for this paper. The authors would like to thank all the organizations for making the data set used in this research available and the School of Marine Science and Technology/University of Massachusetts Dartmouth (SMAST/UMassD) for their support during this research. Danilo A. Silva and Dalton K. Sasaki acknowledge financial support from PETROBRAS (Santos Project, 2018/00068-8), Marcelo Dottori acknowledges support from the Fundação de Amparo à Pesquisa do Estado de São Paulo (FAPESP, 2010/05124-1) and Ilson Carlos Almeida da Silveira acknowledges support from CNPq (Project HIDROSAN I, 405593/2021-0) and FAPESP (Project HIDROSAN II, 2021/13124-6). We also thank the reviewers for their valuable suggestions and comments, which considerably improved the quality of this article. The Article Processing Charge for the publication of this research was funded by the Coordenação de Aperfeiçoamento de Pessoal de Nível Superior - Brasil (CAPES) (ROR identifier: 00x0ma614).

References

Aikman, F. (1984). Pycnocline development and its consequences in the middle Atlantic bight. *Journal of Geophysical Research*, *89*(C1), 685–694. https://doi.org/10.1029/JC089iC01p00685

Alves dos Santos, F., Santi Coimbra de Oliveira, A. L., Mendes Soares, F. L., de Carvalho, G. V., São Tiago, P. M., dos Santos, N. G., et al. (2015). Chapter 7–Projeto azul: Operational oceanography in an active oil and gas area southeastern Brazil. In Y. Liu, H. Kerkering, & R. H. Weisberg (Eds.), *Coastal ocean observing systems* (pp. 99–118). Academic Press. https://doi.org/10.1016/B978-0-12-802022-7.00007-9

ARGO. (2025). Argo float data and metadata from global data assembly centre (Argo gdac) [Dataset]. https://doi.org/10.17882/42182

Belonenko, T. V., Budyansky, M. V., Akhtyamova, A. F., & Udalov, A. A. (2024). Investigation of the Benguela upwelling eddies using Lagrangian modeling methods. *Ocean Dynamics*, *74*(5), 373–390. https://doi.org/10.1007/s10236-024-01609-8

Brink, K. H. (2016). Cross-shelf exchange. *Annual Review of Marine Science*, *8*(1), 59–78. https://doi.org/10.1146/annurev-marine-010814-015717

Brink, K. H. (2026). A numerical study of subsurface salty intrusions onto the continental shelf. *Continental Shelf Research*, *302*, 105746. https://doi.org/10.1016/j.csr.2026.105746

Calado, L., Da Silveira, I., Gangopadhyay, A., & De Castro, B. (2010). Eddy-induced upwelling off cape são tomé (22 s, Brazil). *Continental Shelf Research*, *30*(10–11), 1181–1188. https://doi.org/10.1016/j.csr.2010.03.007

Calado, L., Gangopadhyay, A., & Da Silveira, I. (2006). A parametric model for the Brazil current meanders and eddies off southeastern Brazil. *Geophysical Research Letters*, *33*(12). https://doi.org/10.1029/2006gl026092

21699291, 2026, 11, Downloaded from https://agupubs.onlinelibrary.wiley.com/doi/10.1029/2025JC023411 by Capes, Wiley Online Library on [10/11/2026]. See the Terms and Conditions (https://onlinelibrary.wiley.com/terms-and-conditions) on Wiley Online Library for rules of use; OA articles are governed by the applicable Creative Commons License

Calil, P. H., Suzuki, N., Baschek, B., & da Silveira, I. C. (2021). Filaments, fronts and eddies in the Cabo Frio coastal upwelling system, Brazil. *Fluids*, *6*(2), 54. https://doi.org/10.3390/fluids6020054

Campos, E., Velhote, D., & Silveira, I. D. (2000). Shelf break upwelling driven by Brazil current cyclonic meanders. *Geophysical Research Letters*, *27*(6), 751–754. https://doi.org/10.1029/1999GL010502

Castro, B. M. (2014). Summer/winter stratification variability in the central part of the south Brazil bight. *Continental Shelf Research*, *89*, 15–23. https://doi.org/10.1016/j.csr.2013.12.002

Castro, B. M., & Miranda, L. B. d. (1998). Physical oceanography of the western Atlantic continental shelf located between 4 n and 34 s. *The Sea*, *11*(1), 209–251.

Cerda, C., & Castro, B. M. (2014). Hydrographic climatology of south Brazil bight shelf waters between sao sebastiao (24os) and cabo sao tome (22os). *Continental Shelf Research*, *89*, 5–14. https://doi.org/10.1016/j.csr.2013.11.003

Chen, H., Qi, Y., Wang, Y., & Chai, F. (2019). Seasonal variability of sst fronts and winds on the southeastern continental shelf of Brazil. *Ocean Dynamics 2019*, *69*(11), 1387–1399. https://doi.org/10.1007/S10236-019-01310-1

Chen, K., Gawarkiewicz, G., & Yang, J. (2022). Mesoscale and submesoscale shelf-ocean exchanges initialize an advective marine heatwave. *Journal of Geophysical Research: Oceans*, *127*(1), e2021JC017927. https://doi.org/10.1029/2021JC017927

Clarke, A. J., & Brink, K. (1985). The response of stratified, frictional flow of shelf and slope waters to fluctuating large-scale, low-frequency wind forcing. *Journal of Physical Oceanography*, *15*(4), 439–453. https://doi.org/10.1175/1520-0485(1985)015<0439:trosff>2.0.co;2

CMEMS. (2023a). Global ocean along track l3 sea surface heights reprocessed 1993 ongoing tailored for data assimilation. https://doi.org/10.48670/moi-00146

CMEMS. (2023b). Global ocean gridded l4 sea surface heights and derived variables nrt. https://doi.org/10.48670/moi-00149

CMEMS. (2024a). Global ocean along track l 3 sea surface heights reprocessed 1993 ongoing tailored for data assimilation. *E.U. Copernicus Marine Service Information (CMEMS). Marine Data Store (MDS)*. https://doi.org/10.48670/moi-00146

CMEMS. (2024b). Global ocean gridded l 4 sea surface heights and derived variables reprocessed 1993 ongoing. *E.U. Copernicus Marine Service Information (CMEMS). Marine Data Store (MDS)*. https://doi.org/10.48670/moi-00148

Combes, V., Matano, R. P., & Palma, E. D. (2021). Circulation and cross-shelf exchanges in the northern shelf region of the southwestern Atlantic: Kinematics. *Journal of Geophysical Research: Oceans*, *126*(4), e2020JC016959. https://doi.org/10.1029/2020jc016959

Combes, V., Matano, R. P., & Palma, E. D. (2023). Circulation and cross-shelf exchanges in the northern shelf of the southwestern Atlantic: Dynamics. *Journal of Geophysical Research: Oceans*, *128*(7), e2023JC019887. https://doi.org/10.1029/2023JC019887

Cossarini, G., Querin, S., & Solidoro, C. (2015). The continental shelf carbon pump in the northern Adriatic sea (Mediterranean sea): Influence of wintertime variability. *Ecological Modelling*, *314*, 118–134. https://doi.org/10.1016/j.ecolmodel.2015.07.024

Da Silveira, I., Lima, J., Schmidt, A., Ceccopieri, W., Sartori, A., Franscisco, C., & Fontes, R. (2008). Is the meander growth in the Brazil current system off southeast Brazil due to baroclinic instability? *Dynamics of Atmospheres and Oceans*, *45*(3–4), 187–207. https://doi.org/10.1016/j.dynatmoce.2008.01.002

da Silveira, I., Pereira, F., Flierl, G. R., Simoes-Sousa, I. T., Palóczy, A., Borges-Silva, M., & Rocha, C. B. (2023). The brazil current quasi-stationary unstable meanders at 22°S–23°S. *Progress in Oceanography*, *210*, 102925. https://doi.org/10.1016/j.pocean.2022.102925

Dawson, H. R., Morrison, A. K., England, M. H., & Tamsitt, V. (2023). Pathways and timescales of connectivity around the Antarctic continental shelf. *Journal of Geophysical Research: Oceans*, *128*(2), e2022JC018962. https://doi.org/10.1029/2022jc018962

de Amorim, J. P. M., do Carmo Casseb, A. M., & Martinelli Filho, J. E. (2025). Sargassum transport to the amazon coast: Explaining the stranding through meteorological and oceanographic conditions. *Harmful Algae*, *149*, 102955. https://doi.org/10.1016/j.hal.2025.102955

de Boyer Montégut, C., Madec, G., Fischer, A. S., Lazar, A., & Iudicone, D. (2004). Mixed layer depth over the global ocean: An examination of profile data and a profile-based climatology. *Journal of Geophysical Research*, *109*(C12). https://doi.org/10.1029/2004jc002378

Delandmeter, P., & Van Sebille, E. (2019). The parcels v2. 0 lagrangian framework: New field interpolation schemes. *Geoscientific Model Development*, *12*(8), 3571–3584. https://doi.org/10.5194/gmd-12-3571-2019

Dottori, M., Sasaki, D. K., Silva, D. A., Del-Giovannino, S. R., Pinto, A. P., Gnamah, M., et al. (2023). Hydrographic structure of the continental shelf in santos basin and its causes: The sanagu and sansed campaigns (2019). *Ocean and Coastal Research*, *71*(suppl 3), e23013. https://doi.org/10.1590/2675-2824071.22062md

Emílsson, I. (1961). The shelf and coastal waters off southern Brazil. *Boletim do Instituto Oceanografico*, *11*(2), 101–112. https://doi.org/10.1590/s0373-55241961000100004

Fedorov, A., Budyansky, M., Belonenko, T., Prants, S., Uleysky, M. Y., & Bashmachnikov, I. (2021). Lagrangian modeling of water circulation in the lofoten basin. *Dynamics of Atmospheres and Oceans*, *96*, 101258. https://doi.org/10.1016/j.dynatmoce.2021.101258

Fernandes, F. (2014). python-ctd v0.2.1. *Zenodo*. https://doi.org/10.5281/zenodo.11396

Firing, E., Fernandes, F., Barna, A., & Abernathey, R. (2021). Teos-10/gsw-python: V3.4.1.post0. *Zenodo*. https://doi.org/10.5281/zenodo.5214122

Gangopadhyay, A. (2022). *Introduction to ocean circulation and modeling*. CRC Press.

Gangopadhyay, A., Gawarkiewicz, G., Silva, E. N. S., Monim, M., & Clark, J. (2019). An observed regime shift in the formation of warm core rings from the gulf stream. *Scientific Reports*, *9*(1), 12319. https://doi.org/10.1038/s41598-019-48661-9

Gawarkiewicz, G., Fratantoni, P., Bahr, F., & Ellertson, A. (2022). Increasing frequency of mid-depth salinity maximum intrusions in the middle Atlantic bight. *Journal of Geophysical Research: Oceans*, *127*(7), e2021JC018233. https://doi.org/10.1029/2021jc018233

Gawarkiewicz, G., McCarthy, R. K., Barton, K., Masse, A. K., & Church, T. M. (1990). A gulf stream-derived pycnocline intrusion on the middle Atlantic bight shelf. *Journal of Geophysical Research*, *95*(C12), 22305–22313. https://doi.org/10.1029/JC095iC12p22305

Gawarkiewicz, G., Taenzer, L. L., Silver, A., Ryan, S., Green, E., Gangopadhyay, A., et al. (2025). Mapping of a mid-depth salinity maximum intrusion south of new England in June 2021 and implications for cross-shelf exchange. *Journal of Geophysical Research: Oceans*, *130*(6), e2024JC021536. https://doi.org/10.1029/2024jc021536

Giunta, V., & Ward, B. (2022). Ocean mixed layer depth from dissipation. *Journal of Geophysical Research: Oceans*, *127*(4), e2021JC017904. https://doi.org/10.1029/2021jc017904

González-Pola, C., Ruiz-Villarreal, M., Lavín, A., Cabanas, J. M., & Álvarez Fanjul, E. (2007). A subtropical water intrusion spring-event in the shelf-slope of the south-western Bay of Biscay after strong wind-forcing pulses. *Journal of Atmospheric & Ocean Science*, *10*(4), 343–359. https://doi.org/10.1080/17417530601129148

Gordon, A. L., & Aikman, I. I. I F. (1981). Salinity maximum in the pycnocline of the middle Atlantic bight 1, 2. *Limnology and Oceanography*, *26*(1), 123–130. https://doi.org/10.4319/lo.1981.26.1.0123

Harris, C. R., Millman, K. J., Van Der Walt, S. J., Gommers, R., Virtanen, P., Cournapeau, D., et al. (2020). Array programming with numpy. *Nature*, *585*(7825), 357–362. https://doi.org/10.1038/s41586-020-2649-2

21699291, 2026, 11, Downloaded from https://agupubs.onlinelibrary.wiley.com/doi/10.1029/2025JC023411 by Capes, Wiley Online Library on [10/11/2026]. See the Terms and Conditions (https://onlinelibrary.wiley.com/terms-and-conditions) on Wiley Online Library for rules of use; OA articles are governed by the applicable Creative Commons License

Hersbach, H., Bell, B., Berrisford, P., Biavati, G., Horányi, A., Muñoz Sabater, J., et al. (2018). Era5 hourly data on single levels from 1979 to present. *Copernicus Climate Change Service (C3S) Climate Data Store (CDS)*

Hopkins, J., Sharples, J., & Huthnance, J. M. (2012). On-shelf transport of slope water lenses within the seasonal pycnocline. *Geophysical Research Letters*, *39*(8). https://doi.org/10.1029/2012GL051388

Hoyer, S., & Hamman, J. (2017). Xarray: Nd labeled arrays and datasets in python. *Journal of Open Research Software*, *5*(1), 10. https://doi.org/10.5334/jors.148

Hunter, J. D. (2007). Matplotlib: A 2d graphics environment. *Computing in Science & Engineering*, *9*(3), 90–95. https://doi.org/10.1109/MCSE.2007.55

IFREMER. (2025). Argo float data and metadata from global data assembly centre (Argo gdac). *Institu Français de Recherche pour l'Explotation de la Mer (IFREMER)*. https://doi.org/10.17882/42182

Jean-Michel, L., Eric, G., Romain, B.-B., Gilles, G., Angélique, M., Marie, D., et al. (2021). The copernicus global 1/12 oceanic and sea ice glorys12 reanalysis. *Frontiers in Earth Science*, *9*, 698876. https://doi.org/10.3389/feart.2021.698876

Lentz, S. J. (2003). A climatology of salty intrusions over the continental shelf from georges bank to cape hatteras. *Journal of Geophysical Research*, *108*(C10). https://doi.org/10.1029/2003jc001859

Lentz, S. J., & Chapman, D. C. (2004). The importance of nonlinear cross-shelf momentum flux during wind-driven coastal upwelling. *Journal of Geophysical Research*, *34*(11), 2444–2457. https://doi.org/10.1175/JPO2644.1

Li, Y., Wang, F., & Sun, Y. (2012). Low-frequency spiciness variations in the tropical Pacific Ocean observed during 2003–2012. *Geophysical Research Letters*, *39*(23). https://doi.org/10.1029/2012GL053971

Liu, K.-K., Atkinson, L., Quiñones, R., & Talaue-McManus, L. (2010). *Carbon and nutrient fluxes in continental margins: A global synthesis*. Springer Science & Business Media.

Lorbacher, K., Dommenget, D., Niiler, P., & Köhl, A. (2006). Ocean mixed layer depth: A subsurface proxy of ocean-atmosphere variability. *Journal of Geophysical Research*, *111*(C7). https://doi.org/10.1029/2003jc002157

Luko, C. D., Pereira, F., da Silveira, I. C., Tandon, A., & Flierl, G. R. (2022). Effects of the seasonality of mesoscale eddies on the planktonic dynamics off eastern Brazil. *Dynamics of Atmospheres and Oceans*, *98*, 101299. https://doi.org/10.1016/j.dynatmoce.2022.101299

Malan, N., Archer, M., Roughan, M., Cetina-Heredia, P., Hemming, M., Rocha, C., et al. (2020). Eddy-driven cross-shelf transport in the east Australian current separation zone. *Journal of Geophysical Research: Oceans*, *125*(2), e2019JC015613. https://doi.org/10.1029/2019JC015613

Mascarenhas Jr, A. D. S., Miranda, L. d., & Rock, N. (1971). A study of the oceanographic conditions in the region of Cabo Frio. *Fertility of the Sea*, *1*, 285–308.

Mason, E., Pascual, A., & McWilliams, J. C. (2014). A new sea surface height–based code for oceanic mesoscale eddy tracking. *Journal of Atmospheric and Oceanic Technology*, *31*(5), 1181–1188. https://doi.org/10.1175/jtech-d-14-00019.1

Maze, G., & Balem, K. (2020). Argopy: A python library for argo ocean data analysis. *Journal of Open Source Software*, *5*(53), 2425. https://doi.org/10.21105/joss.02425

McDougall, T. J., & Barker, P. M. (2011). Getting started with teos-10 and the Gibbs seawater (gsw) oceanographic toolbox. *Scor/Iapso WG*, *127*(532), 1–28.

Moreira, D. L., Dalto, A. G., Figueiredo Jr, A. G., Valerio, A. M., Detoni, A., Bonecker, A. C., et al. (2023). Multidisciplinary scientific cruises for environmental characterization in the Santos basin–methods and sampling design. *Ocean and Coastal Research*, *71*(suppl 3), e23022. https://doi.org/10.1590/2675-2824071.22072dlm

Namiki, C., Katsuragawa, M., Napolitano, D. C., de Lourdes Zani-Teixeira, M., de Mattos, R. A., & da Silveira, I. C. A. (2017). Hydrodynamically-driven distribution of lanternfish larvae in the southeast Brazilian bight. *Journal of Marine Systems*, *170*, 115–133. https://doi.org/10.1016/J.JMARSYS.2017.02.006

Oliveira, R., Pezzi, L. P., Souza, R. B. d., Santini, M. F., Cunha, L., & Pacheco, F. S. (2019). First measurements of the ocean-atmosphere co2 fluxes at the cabo frio upwelling system region, southwestern Atlantic Ocean. *Continental Shelf Research*, *181*, 135–142. https://doi.org/10.1016/j.csr.2019.05.008

Palóczy, A., Brink, K. H., da Silveira, I. C., Arruda, W. Z., & Martins, R. P. (2016). Pathways and mechanisms of offshore water intrusions on the espírito santo basin shelf (18°S–22°S, Brazil). *Journal of Geophysical Research: Oceans*, *121*, 5134–75163. https://doi.org/10.1002/2015JC011468

Pegliasco, C., Delepoulle, A., Mason, E., Morrow, R., Faugère, Y., & Dibarboure, G. (2022). Meta3. 1exp: A new global mesoscale eddy trajectory atlas derived from altimetry. *Earth System Science Data*, *14*(3), 1087–1107. https://doi.org/10.5194/essd-14-1087-2022

Pereira, F., Bouali, M., Polito, P. S., Da Silveira, I., & Candella, R. N. (2020). Discrepancies between satellite-derived and in situ sst data in the cape frio upwelling system, southeastern Brazil (23°S). *Remote Sensing Letters*, *11*(6), 555–562. https://doi.org/10.1080/2150704x.2020.1742941

Pimenta, F. M., Silva, A. R., Assireu, A. T., Almeida, V. d. S. e., & Saavedra, O. R. (2019). Brazil offshore wind resources and atmospheric surface layer stability. *Energies*, *12*(21), 4195. https://doi.org/10.3390/en12214195

Posmentier, E. S., & Houghton, R. W. (1978). Fine structure instabilities induced by double diffusion in the shelf/slope water front. *Journal of Geophysical Research*, *83*(C10), 5135–5138. https://doi.org/10.1029/JC083IC10P05135

Reijnders, D., Denes, M. C., Rühs, S., Breivik, Ø., Nordam, T., & van Sebille, E. (2026). Stability bias in lagrangian (back) tracking in divergent flows. *Journal of Advances in Modeling Earth Systems*, *18*(1), e2025MS005470. https://doi.org/10.1029/2025ms005470

Rocha, C. B., & Simoes-Sousa, I. T. (2022). Compact mesoscale eddies in the south Brazil bight. *Remote Sensing*, *14*(22), 5781. https://doi.org/10.3390/rs14225781

Rozante, J. R., Moreira, D. S., de Goncalves, L. G. G., & Vila, D. A. (2010). Combining trmm and surface observations of precipitation: Technique and validation over South America. *Weather and Forecasting*, *25*(3), 885–894. https://doi.org/10.1175/2010waf2222325.1

Ruddick, B., & Kerr, O. (2003). Oceanic thermohaline intrusions: Theory. *Progress in Oceanography*, *56*(3–4), 483–497. https://doi.org/10.1016/s0079-6611(03)00029-6

Ruiz-Castillo, E., Sharples, J., Hopkins, J., & Woodward, M. (2019). Seasonality in the cross-shelf physical structure of a temperate shelf sea and the implications for nitrate supply. *Progress in Oceanography*, *177*, 101985. https://doi.org/10.1016/j.pocean.2018.07.006

Saha, K., Zhao, X., Zhang, H.-m., Casey, K. S., Zhang, D., Baker-Yeboah, S., et al. (2018). *AVHRR pathfinder version 5.3 level 3 collated (l3c) global 4km sea surface temperature for 1981-present*. NOAA National Centers for Environmental Information.

Sasaki, D. K., Silva, D., Del Giovannino Júnior, S. R., Almeida da Silveira, I. C., Belo, W. C., Martins, R. P., & Dottori, M. (2024). Hydrographic climatology of the south Brazil bight continental shelf and slope. *Theoretical and Applied Climatology*, *155*(10), 9407–9425. https://doi.org/10.1007/s00704-024-05144-w

21699291, 2026, 11, Downloaded from https://agupubs.onlinelibrary.wiley.com/doi/10.1029/2025JC023411 by Capes, Wiley Online Library on [10/11/2026]. See the Terms and Conditions (https://onlinelibrary.wiley.com/terms-and-conditions) on Wiley Online Library for rules of use; OA articles are governed by the applicable Creative Commons License

Seijo-Ellis, G., Giglio, D., & Salmun, H. (2023). Intrusions of Amazon River waters in the Virgin Islands basin during 2007–2017. *Journal of Geophysical Research: Oceans*, *128*(3), e2022JC018709. https://doi.org/10.1029/2022jc018709

Silva, D. A. (2024). *Cross-shelf exchanges: Subsurface salinity maximum in the south Brazil bight*. Institute of Oceanography, University of São Paulo. https://doi.org/10.11606/T.21.2024.tde-24102024-154705

Silva, D. A., Sasaki, D. K., Dottori, M., da Silveira, I. C. A., Belo, W. C., & Martins, R. P. (2023). An inventory of salty and warm subsurface intrusions in the south Brazil bight. *Continental Shelf Research*, *259*, 104984. https://doi.org/10.1016/j.csr.2023.104984

Silver, A., Gangopadhyay, A., Gawarkiewicz, G., Andres, M., Flierl, G., & Clark, J. (2022). Spatial variability of movement, structure, and formation of warm core rings in the northwest Atlantic slope sea. *Journal of Geophysical Research: Oceans*, *127*(8), e2022JC018737. https://doi.org/10.1029/2022jc018737

Silver, A., Gangopadhyay, A., Gawarkiewicz, G., Fratantoni, P., & Clark, J. (2023). Increased gulf stream warm core ring formations contributes to an observed increase in salinity maximum intrusions on the northeast shelf. *Scientific Reports*, *13*(1), 1–9. https://doi.org/10.1038/s41598-023-34494-0

Stech, J. (1990). *Um estudo comparativo da dinâmica da circulação de inverno entre as plataformas continentais das costas sudeste do brasil e dos estados unidos utilizando um modelo numérico*. São Paulo.

Stern, M. E. (1967). Lateral mixing of water masses. *Deep Sea Research and Oceanographic Abstracts*, *14*(6), 747–12753. https://doi.org/10.1016/S0011-7471(67)80011-1

Uchoa, I., Simoes-Sousa, I. T., & da Silveira, I. C. (2023). The Brazil current mesoscale eddies: Altimetry-based characterization and tracking. *Deep Sea Research Part I: Oceanographic Research Papers*, *192*, 103947. https://doi.org/10.1016/j.dsr.2022.103947

Vallès-Casanova, I., Fraile-Nuez, E., Martín-Rey, M., van Sebille, E., Cabré, A., Olivé-Abelló, A., & Pelegrí, J. L. (2022). Water mass transports and pathways in the north brazil-equatorial undercurrent retroflection. *Journal of Geophysical Research: Oceans*, *127*(5), e2021JC018150. https://doi.org/10.1029/2021jc018150

Vilanova, G., de Lourdes Zani-Teixeira, M., Katsuragawa, M., dos Santos, U. C., Dottori, M., Silva, D. A., et al. (2026). Water mass influence on the distribution of larval mesopelagic fish (sternoptychidae) in the south Brazil bight (23°S–28°S). *Journal of Marine Systems*, 104185. https://doi.org/10.1016/j.jmarsys.2026.104185

Wang, D. P., & Jordi, A. (2011). Surface frontogenesis and thermohaline intrusion in a shelfbreak front. *Ocean Modelling*, *38*(1–2), 161–170. https://doi.org/10.1016/J.OCEMOD.2011.02.012

Weatherall, P., Marks, K. M., Jakobsson, M., Schmitt, T., Tani, S., Arndt, J. E., et al. (2015). A new digital bathymetric model of the world's oceans. *Earth and space Science*, *2*(8), 331–345. https://doi.org/10.1002/2015ea000107

Zembruscki, S. G. (1979). Geomorfologia da margem continental sul brasileira e das bacias oceânicas adjacentes. *PETROBRAS. CENPES. DINTEP (Série Projeto REMAC NUM. 7)*.

21699291, 2026, 11, Downloaded from https://agupubs.onlinelibrary.wiley.com/doi/10.1029/2025JC023411 by Capes, Wiley Online Library on [10/11/2026]. See the Terms and Conditions (https://onlinelibrary.wiley.com/terms-and-conditions) on Wiley Online Library for rules of use; OA articles are governed by the applicable Creative Commons License